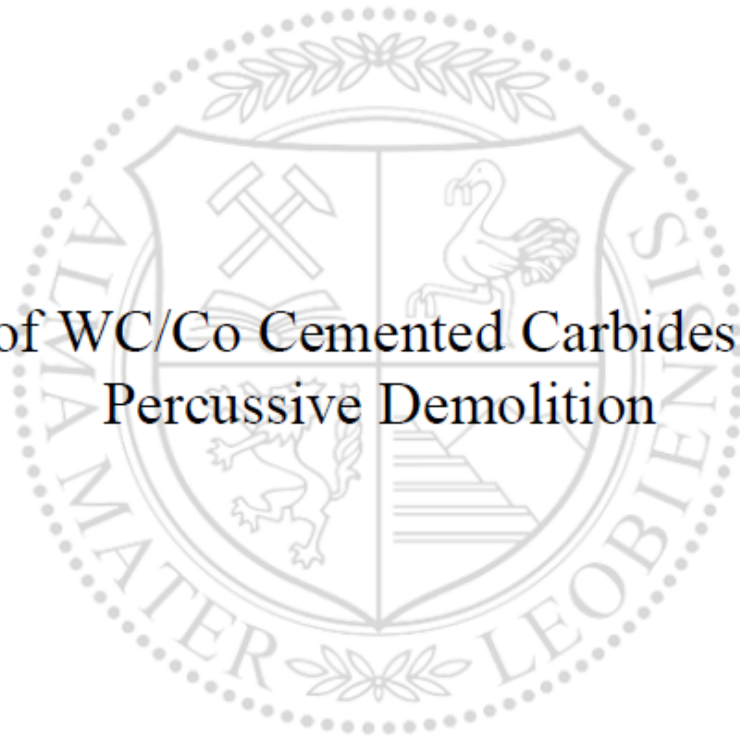




Chair of Structural and Functional Ceramics

Master's Thesis

Wear of WC/Co Cemented Carbides during
Percussive Demolition



Matthias Freisinger, BSc

April 2019

The present work was processed at HILTI AG headquarter in Schaan / Liechtenstein (April to September 2018), in cooperation with the Chair of Structural and Functional Ceramics of the Montanuniversität in Leoben.



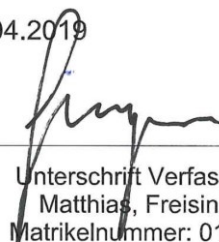
EIDESSTÄTTLICHE ERKLÄRUNG

Ich erkläre an Eides statt, dass ich diese Arbeit selbstständig verfasst, andere als die angegebenen Quellen und Hilfsmittel nicht benutzt, und mich auch sonst keiner unerlaubten Hilfsmittel bedient habe.

Ich erkläre, dass ich die Richtlinien des Senates der Montanuniversität Leoben zu "Gute wissenschaftliche Praxis" gelesen, verstanden und befolgt habe.

Weiters erkläre ich, dass die elektronische und gedruckte Version der eingereichten wissenschaftlichen Abschlussarbeit formal und inhaltlich identisch sind.

Datum 12.04.2019



Unterschrift Verfasser/in
Matthias, Freisinger
Matrikelnummer: 01035149

DANKSAGUNG

Als Erstes möchte ich mich bei meinen Betreuern, o. Univ. Prof. Dr. Robert Danzer und Dr. Walter Harrer, vom Lehrstuhl für Struktur- und Funktionskeramik Leoben an der Montanuniversität Leoben für das Ermöglichen dieser Diplomarbeit sowie die großartige Unterstützung und Betreuung herzlich bedanken.

Einen besonderen Dank möchte ich meiner Betreuerin Dr. Patricia Alveen für ihre hervorragende Betreuung in der CR&T TMM Gruppe der Firma HILTI in Schaan aussprechen, die mir ein selbstbestimmtes und kreatives Arbeiten ermöglichte und gleichzeitig immer zur Stelle war, falls es notwendig war. Dadurch konnte ich mich in diesen sechs Monaten immens weiterentwickeln, sowohl auf fachlicher als auch auf persönlicher Ebene. Des Weiteren möchte ich mich bei Dr. Steven Moseley und Dr. Siavash Momeni für die fachliche Unterstützung, sowie bei allen Teammitgliedern der Metallographie für deren Herzlichkeit, Hilfe und die gute Zusammenarbeit bedanken.

Ein spezieller Dank geht an meine Freunde, welche einen grundlegenden Teil meines Lebens bilden. Ich bin sehr dankbar für die neu gewonnenen Freundschaften während meiner Zeit im "Ländle" (Antonio, Cien, David, Fabian, Georg, Julia, Leon, Marco, Nathan, Sandra, Tina) - ich freue mich bereits, euch alle wiederzusehen. Ich möchte mich auch bei meinen Freunden bedanken, welche ich in Leoben kennengelernt habe (Andi, Flo, Fredi, Ingolf, Lisa, Martin B., Martin S., Resi, Ruth, Seppi, Simon F., Simon N., Tiago, Thomas) - danke für eure Unterstützung und die schöne Zeit, mit vielen unvergesslichen Momenten. Zu guter Letzt möchte ich mich bei meinen langjährigen Freunden aus meiner Heimat bedanken (Andi, Anja, Felix, Kathrin, Katja, Kerstin, Klaus, Luki, Martina, Michi, Reisi, Sabine, Thomas) - ich schätze euch sehr und bin stolz darauf, dass wir immer für einander da sind.

Ein besonderer Dank gilt auch meiner Freundin Sara. Danke für deine Liebe und den Rückhalt, den du mir gibst. Danke auch für deine Abenteuerlust am 12. August.

Schlussendlich möchte ich meiner Familie danken. Danke an meinen Onkel Gusti für das Rasenmähen während meiner Zeit in Liechtenstein, und bei meiner Oma Elvira für ihre langjährige Unterstützung. Ein großes Dankeschön an meine Schwester Carina für ihre wertvolle Unterstützung, ich schätze unseren Zusammenhalt wirklich sehr.

Mein größter Dank gebührt meinem Vater, Gerhard Freisinger. Ohne deine Unterstützung, dein offenes Ohr, deine Ratschläge und der Tatsache, dass du immer hinter mir stehst, egal welchen Weg ich gehe, wäre ich nicht da, wo ich heute bin.

ACKNOWLEDGEMENTS

To begin with, I would like to thank my supervisors, o. Univ. Prof. Dr. Robert Danzer and Dr. Walter Harrer, from the “Lehrstuhl für Struktur- und Funktionskermamik Leoben” at the Montanuniversity Leoben for making this thesis possible and their great help and support.

I would like to express a special thanks and appreciation to my supervisor Dr. Patricia Alveen for her excellent leadership at the CR&T TMM group at HILTI Headquarter in Schaan, which gave me the opportunity to be creative and independent during my work without missing support at any time. This enabled me to grow during these six months by improving my professional abilities, but also my soft skills. Furthermore, I would like to thank Dr. Steven Moseley and Dr. Siavash Momeni for their specialist support, as well as the team members of the Metallography for their friendliness and cooperativeness.

I would like to address particular words of thanks to all my friends which are essential parts of my life. First, I am grateful for the arisen friendships during my time in the “Ländle” (Antonio, Cien, David, Fabian, Georg, Julia, Leon, Marco, Nathan, Sandra, Tina) - I am looking forward to meet all of you again. Next, I would like to thank my friends who I have got to know during my time in Leoben (Andi, Flo, Fredi, Ingolf, Lisa, Martin B., Martin S., Ruth, Seppi, Simon F., Simon N., Tiago, Thomas) - thank you for your support and the numerous delightful memories. Last but not least, I would like to say a special word of thanks to my lifelong friends of my home area (Andi, Anja, Felix, Kathrin, Katja, Kerstin, Klaus, Luki, Martina, Michi, Reisi, Sabine, Thomas) - I really appreciate you for being there for one another no matter what or when.

A special thanks to my girlfriend Sara for her love and tremendous encouragement, but also for her spirit of adventure, particularly on August 12.

Finally, I would like to thank my family. Special thanks to my uncle Gusti for mowing the lawn during my stay in Liechtenstein and to my grandmother Elvira for her support over all these years. Big thanks to my sister Carina for her valuable support, I really appreciate our close connection.

My greatest thanks go to my father, Gerhard Freisinger, making this all possible. Without your guidance and support, your open ear and advices, and your approach to always stand behind me, no matter what decision I am making, I would not be who I am today.

KURZFASSUNG

Verschleiß von WC/Co Hartmetallen unter schlagender Belastung

Diese Diplomarbeit beschäftigt sich mit dem Verschleiß und den unterschiedlichen Verschleißmechanismen von WC/Co Hartmetallen unter schlagender Belastung, auch Meißeln genannt. Zehn verschiedene Materialsorten, unterschiedlich in Bezug auf Karbidkorngröße und Bindergehalt, wurden betrachtet. Das Hauptziel war es, verschiedene Testvarianten zu evaluieren und Zusammenhänge zwischen diesen und dem Verschleiß unterschiedlicher Hartmetallsorten zu finden. Ebenfalls wurden verschleißene Hartmetallspitzen des HILTI Stockerwerkzeuges analysiert und mit den Ergebnissen der Labor- und Versuchstandtests verglichen. Weiters wurden die Korngrößenverteilungen und mechanische Eigenschaften, wie Härte und Palmqvist Bruchzähigkeit, der Hartmetallsorten untersucht. Der LCPC Verschleißtest wurde durchgeführt und eine eindeutige Korrelation zur Härte der Werkstoffe aufgezeigt. Realitätsnahe Tests der Hartmetallspitzen wurden in einem vollautomatisierten 3-Achsen Versuchstand durchgeführt. Es konnten klare Zusammenhänge zwischen den Labortests und den untersuchten HILTI Stockerwerkzeugen aufgezeigt werden. Ausführliche makro- und mikroskopische Analysen stellten das Verschleißverhalten und unterschiedliche Verschleißmechanismen der Hartmetallspitzen dar. Es konnte gezeigt werden, dass im Bereich der Spitzen hauptsächlich Zerüttung, vor allem das Ausbrechen größerer Karbidkörnersegmente und das Loslösen ganzer Segmente, stattfindet. Im Bereich der Seitenflächen ist der dominierende Verschleißmechanismus der abrasive Verschleiß. Tendenziell zeigten sich hier abgerundete Karbidkörner und weniger Risse. Des Weiteren konnten Zusammenhänge in Bezug auf Verschleiß zwischen WC/Co Sorten, Probengeometrien und Testmethoden beschrieben werden.

ABSTRACT

Wear of WC/Co Cemented Carbides during Percussive Demolition

This work investigates the wear behavior and mechanisms of WC/Co cemented carbides during percussive demolition. Ten different material grades, varying in regards of carbide grain size and binder content, were selected. The main objective was to evaluate different testing methods and to find correlations. Additionally, worn cemented carbide pins of the HILTI bushing tool were analyzed and these results were compared to the results of the laboratory and application tests. The cemented carbide grades were investigated concerning their grain size distribution and their mechanical properties, namely hardness and Palmqvist fracture toughness. The laboratory LCPC wear test was executed and a clear correlation to hardness was shown. The application testing was done in a fully-automated 3 axis test rig and revealed significant correlations to the laboratory testing as well as to the analyzed HILTI bushing tools. Extensive macroscopic and microscopic analysis such as Scanning Electron Microscopy were done to identify different wear mechanisms. The detected wear mechanism at the tip area was mainly impact spalling, most notably the detachment of whole WC grains and composite scale fragments. At the side area of the cemented carbide pins grinding abrasion seemed to be the dominant wear mechanism. Correlations between different WC/Co grades, sample geometries and testing methods were described in detail.

TABLE OF CONTENTS

EIDESSTÄTLICHE ERKLÄRUNG	I
DANKSAGUNG	II
ACKNOWLEDGEMENTS	III
KURZFASSUNG.....	IV
ABSTRACT	V
TABLE OF CONTENTS.....	VI
1 INTRODUCTION	1
1.1 Project Objectives and Thesis Outline	1
1.2 Cemented Carbides	2
1.3 Wear	4
2 MATERIALS.....	6
2.1 WC/Co Cemented Carbides.....	6
2.1.1 Mechanical Properties of WC/Co Cemented Carbides.....	6
2.1.2 Wear Mechanisms of WC/Co Cemented Carbides	9
2.2 Concrete	13
2.3 Granite	14
3 TESTING METHODS.....	15
3.1 Fracture Toughness Measurement	15
3.2 Edge Toughness Test.....	16
3.3 LCPC Test	18
3.4 Application Testing.....	20
4 ANALYSIS METHODS.....	21
4.1 Macroscopic Analysis Methods.....	22
4.2 Microscopic Analysis Methods	23

5	RESULTS AND DISCUSSION	24
5.1	Grain Size Distribution	27
5.2	Mechanical Properties.....	29
5.2.1	Hardness and Palmqvist Fracture Toughness	29
5.2.2	Edge Toughness	30
5.2.3	Discussion of the results.....	33
5.3	LCPC Wear Test.....	34
5.3.1	Discussion of the results.....	36
5.4	Application Testing.....	37
5.4.1	Discussion of the results.....	47
5.5	Analysis of the HILTI bushing tool.....	49
5.5.1	Discussion of the results.....	53
6	SUMMARY, CONCLUSION AND FUTURE WORK	54
6.1	Summary of the Results and Conclusions	54
6.2	Future Work	56
7	REFERENCES	57
	LIST OF TABLES	61
	LIST OF FIGURES	62
	ANNEXES	65

ACRONYMS AND ABBREVIATIONS

BSE	Backscattered Electrons
CCD	Charged Coupled Device
EDX	Energy Dispersive X-Ray
fcc	face-centered cubic
GK32	Größtkorn 32mm
hcp	hexagonal close packed
K_{Ic}	plane strain fracture toughness
LOM	Light Optical Microscope
SE	Secondary Electrons
SEM	Scanning Electron Microscope
WC/Co	Tungsten Carbide Cobalt
wt%	Weight percent

1 Introduction

1.1 Project Objectives and Thesis Outline

Cemented carbides, used for example for rock drilling, mining applications and demolishing tools, exhibit a very complex situation regarding its wear behavior. Even though numerous studies have been done in recent decades, the countless influencing parameters lead to almost inexhaustible topics for studies, moreover, increasing demands in technical applications underline the importance of these.

A closer look at the field of rock drilling reveals that the influence of different parameters on the wear behavior is tremendous, ranging from different drilling techniques, cutting materials and rock types, to environmental influences like temperature. Most of the studies in this field have been done on rotary/percussive drilling since this is the most common drilling technique in mining operations.

In this work a closer look at percussive demolishing is taken, specifically on the wear of cemented carbide parts for that application. Cemented carbides are widely used due to their outstanding combination of properties, more specifically a high hardness due to the hard carbide phase and a high toughness because of the soft metal binder phase. A commonly used type of cemented carbide for rock drilling and similar applications is WC/Co. The influence of the tungsten carbide grain size and the cobalt binder content on the properties of this composite material is vital. Hence, different WC/Co grades are tested and analyzed in this work.

The main objective of the project is to use different test methods to compare the defined WC/Co grades among each other in terms of wear behavior, furthermore trying to relate these tests to each other. The main analysis method is the Light Optical and Scanning Electron Microscope to investigate the different wear behavior which, due the fact that several wear mechanisms take place simultaneously and they are overlapping each other, presents itself as a serious challenge.

1.2 Cemented Carbides

Cemented Carbides, also referred to as hard metals, are composite materials consisting of hard refractory carbides of the transition metals (for instance WC, TiC or TaC) and a tough binder metal (such as cobalt or nickel) [1]. A representative image of the microstructure of cemented carbide is shown in Figure 1. They are manufactured by powder metallurgy which implies the mixing of the powder of the carbide together with the metal powder, the pressing process and the sintering of the compacted body.

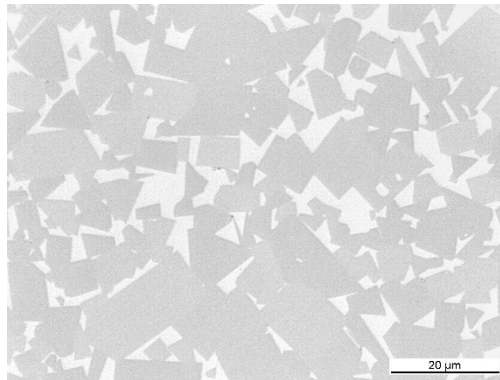


Figure 1: Microstructure of WC-9.5 wt% Co cemented carbide

The origin of this material group date back to the early years of the 20th century when drawing dies from tungsten carbide were successfully produced in Germany. The next step, and the breakthrough for the success story of cemented carbides, was reached in the early 1920s by mixing tungsten carbide and cobalt powder, compacting and heating them above the melting temperature of cobalt. Since then, a lot of studies have been done and numerous other combinations of a hard carbide phase and a metal binder have been developed. [1]

Due to the combination of two different types of materials, cemented carbides show outstanding mechanical properties, more precisely a high hardness and wear resistance, due to the carbide phase, as well as a high toughness, because of the ductile binder phase, not to mention the chemical stability. Thus, these composite materials are very popular and showing a wide range of applications in the field of metal machining and rock drilling, particularly geological exploration, mine excavation and oil drilling [2]. For the latter, the cemented carbide buttons may also be covered by polycrystalline diamond to extend the lifetime [3], but still, regarding common rock drilling one category of cemented carbides is dominant, namely WC/Co. This type of cemented carbide consists of the hard but brittle tungsten carbide phase and a tough cobalt binder phase. Typical drill bits with cemented carbide buttons for rotary percussion drilling, which are used for oil drilling or water well drilling, are shown in Figure 2.



Figure 2: Drill bits for rotary percussion drilling [2]

In general, the mechanical properties of cemented carbides are strongly affected by the size of the carbide grains and the content of the binder, hence, these parameters need to be chosen carefully to achieve a good balance between wear resistance and fracture toughness. The most commonly used WC/Co grades for rock drilling have a WC grain size of 2-5 μm and an amount of Co binder between 5 to 10 wt% [4]. The most widely used technique in rock drilling is rotary/percussive drilling, however, cemented carbides are also used for other demolishing techniques. As an example of a purely percussive demolishing technique the so-called HILTI bushing tool shall be mentioned (shown in Figure 3). This kind of chisel can be used with a percussion drill to roughening up surfaces, to remove excess concrete and to level concrete surfaces. To withstand high percussive strain and to ensure a high durability, WC/Co is successfully used for the pins on the HILTI bushing tool head.



Figure 3: HILTI bushing tool with cemented carbide pins

1.3 Wear

Wear is defined as “the damage to a solid surface, generally involving progressive loss of material, due to relative motion between that surface and a contacting substance or substances” [5].

Even though the first documented observations of this phenomenon were in the first century BC [6], the studies of wear have intensified in the industrial era, especially due to the requirements of the machines in the industrial sector and the field of mechanical engineering during the early 20th century. Since then, numerous different classification schemes have been developed based on different classifying criteria. Here it is worth mentioning the classification suggested by Siebel in 1938, which is based on different types of relative motion, the classification of wear which relied on the scale of surface damage by Archard and Hirst in 1956 and the classification by Burwell in 1958. [7]

The latter is quite common, in which the different types of wear are summarized into five categories by [7], which are as follows:

1. Adhesive or galling wear
2. Abrasive and cutting wear
3. Corrosive wear
4. Surface fatigue
5. Minor types of wear

Some more suggestions for the classification of wear were published by Kostetskii et al. in 1976, by Czichos in 1978 and by Lim and Ashby in 1987, and lastly by Varenberg who made a classification where all these different suggestions are cumulated (shown in Figure 4). [8]








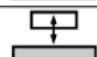

Surface disturbance Relative motion	Generation of defects		Generation of heat	
	 Storage of defects	 Motion of defects	 Chemical interaction	 Physical interaction
 Fretting	Fretting fatigue	Fretting wear		
 Sliding	Fatigue wear	Abrasive wear		Adhesive wear
 Rolling	Pitting	Solid-particle crushing		
 Impact	Impact wear			
 Flow	Liquid-impact erosion	Solid-particle erosion		Ablation erosion

Figure 4: Summary of pathological wear types determined by relative motion and surface disturbance by [8].

Depending on a variety of parameters, for instance mechanical loads, environmental conditions and temperature, multiple types of wear may occur simultaneously. Furthermore, every wear type can show several wear mechanisms, hence, the study of wear demonstrates a high level of complexity.

Regarding the topic of rock drilling, the wear of the cemented carbide parts, disregarding the different drilling techniques, can be described referring to [9] by the following most important mechanisms:

1. Surface impact spalling
2. Surface impact fatigue spalling
3. Thermal fatigue
4. Abrasion

Wear of rock-drilling tools decreases penetration rates, increases the drilling forces and may finally lead to a complete fracture of the insert [9]. Therefore, the knowledge about the occurring wear mechanisms in a specific application is vital, even though overlapping and different wear mechanisms, depending on the process parameters as well as the rock type, makes the determination a major challenge.

2 Materials

2.1 WC/Co Cemented Carbides

Even though multiple different combinations of a hard phase and a metal binder have been developed in recent decades, for example titanium carbides or tantalum carbides combined with a nickel or iron binder, WC/Co is still the most widely used cemented carbide in technical applications like rock drilling or cutting applications. [10]

On that account, different grades of WC/Co cemented carbides have been investigated in this work in terms of its wear behavior.

2.1.1 Mechanical Properties of WC/Co Cemented Carbides

Pertaining to the mechanical properties of cemented carbides, all is based on the combination of a hard carbide phase and a ductile binder material. Hence, this composite material shows the typical properties of ceramics, such as high hardness and chemical stability, as well as typical metal properties, like relative high toughness and good thermal conductivity. Due to the possibility to use different grain sizes of WC and to vary the amount of Co binder, the materials exhibit a wide range of mechanical properties. In the following sections a closer look at hardness and fracture toughness of WC/Co cemented carbides is taken.

Due to the much higher amount of WC (70-97 wt%) than the binder, it is obvious that the hardness of WC/Co cemented carbides is primarily accounted for by the tungsten carbide phase. The crystal structure of WC is non-centrosymmetric hexagonal (shown in Figure 5), therefore the hardness is dependent on the crystal orientation, resulting in a hardness value of 1300 HV on the crystal prism planes and 2300 HV on the basal plane [11].

The crystal structure of the Co binder in WC/Co cemented carbides is the ductile β -phase (fcc), the so-called high temperature phase, which can be stabilized by alloying elements like Ni to counteract the transition to its brittle low temperature phase (hcp) [12]. The bulk hardness of the cobalt phase is below 100 HV, but nanoindentation tests have shown that the Co binder right next to the carbide grains is four times harder than in case of the bulk [13].

As previously mentioned, the tungsten carbide phase is the main reason for the hardness of WC/Co cemented carbides, with the main contributing factors being the volume fraction and the particle size of the WC phase [14]. With decreasing volume fraction of the carbide phase, thus an increasing cobalt binder content, the hardness decreases. Furthermore, if the particle size of the WC phase, also referred to as the carbide grain size, decreases, the hardness increases. These correlations are plotted in Figure 6.

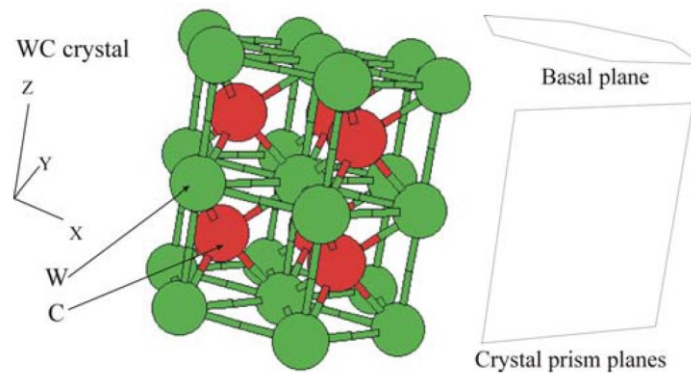


Figure 5: The hexagonal WC crystal structure [15].

Owing to the possibility to adapt the tungsten carbide grain size, as well as the volume fraction, a wide hardness spectrum for WC/Co cemented carbides can be observed, for example a WC/Co grade with 25 wt% Co content and 5 μm WC grains has an approximately hardness of 700 HV, in contrast to a grade with 5 wt% Co and submicron WC grain size with a hardness of around 2200 HV [15].

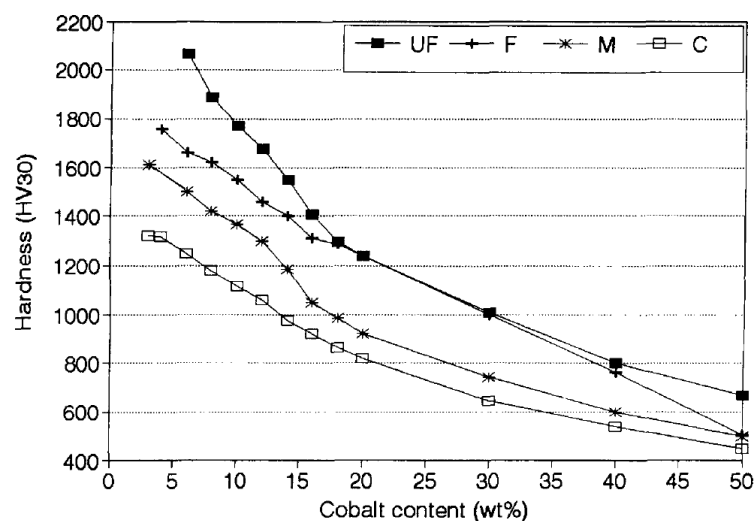


Figure 6: Plots of the hardness of different WC-Co grades vs the cobalt content, at approximately constant grain size. The grain size of the tungsten carbides is classified in UF (ultra-fine), F (fine), M (medium) and C (coarse) [16].

Fracture toughness, related to the resistance to crack propagation, is one of the most beneficial mechanical properties of cemented carbides. The ductile metal binder phase is responsible for the high toughness values of cemented carbides, generally indicated by K_{Ic} , the plane strain fracture toughness.

Hence, the main influencing parameter on this mechanical property is the volumetric percentage of the binder phase, leading in general to an increasing fracture toughness of cemented carbides with higher binder amount. This is based on the ductile nature of the metallic binder, which allows it to absorb energy and plastically deform. Furthermore, the grain size of the carbide grains also reveals a correlation to the toughness, more precisely a coarser WC phase increases the fracture toughness. Consequently, it reveals the inverse relation with respect to hardness, which is also shown in Figure 7. [17]

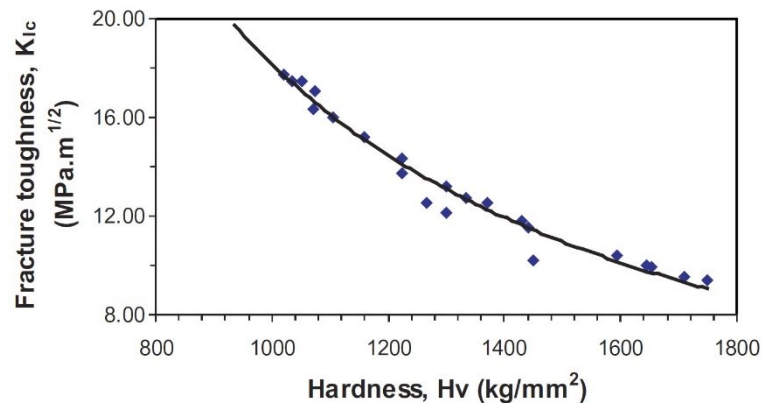


Figure 7: Correlation between fracture toughness and hardness for WC/Co cemented carbides [17].

A further, very important, mechanical property is the so-called transverse rupture strength (TRS), which is kind of a combination of shear strength, compressive strength, and tensile strength [10].

In the industry, it is often loosely equaled to toughness, but in contrast to the correlation between hardness and fracture toughness, the TRS shows a quite different correlation. At lower hardness values of the cemented carbide, the TRS appears to increase since a certain peak value of the hardness, and then decrease as the hardness further increases (see Figure 8). Common values for WC/Co cemented carbides are in between 2000 and 4000 MPa. [17]

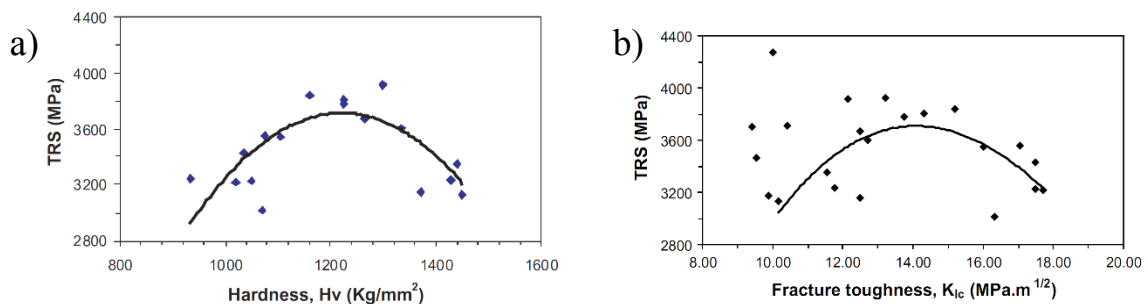


Figure 8: Correlations between TRS and a) hardness, and b) fracture toughness [17].

Even though the density is a physical property, it should be mentioned at the end of this section. The typical density of cemented carbides is about 13 – 15 g/cm³, which is twice the density of steel and 5 – 6 times the density of granite [15]. The density of the pure tungsten carbide is 15.7 g/cm³ and for the cobalt 8.8 g/cm³ [18].

2.1.2 Wear Mechanisms of WC/Co Cemented Carbides

In this thesis, the wear mechanisms of WC/Co cemented carbides during pure percussive demolition without a rotary movement are investigated, to examine their performance during chiseling. However, almost all studies in wear mechanisms of cemented carbides have been done on rotary/percussive drilling. That is because the rotary/percussive drilling is the most widespread demolition technique in the field of mining operations. Nevertheless, some of the individual wear mechanisms occurring are likely the same, therefore an overview of former studies about wear of cemented carbides in rock drilling is given in this section.

Even though this issue has been the topic of numerous different studies during the last several decades, varied rock types and wear measurement methods are a significant barrier to get a clear overview. One further obstacle is the diversity of the presented names for the wear mechanisms. [15]

In 1968, the wear of drill bits used in rotary/percussive demolishing was investigated by Montgomery [19], resulting in the conclusion that the main wear mechanism is fatigue micro-spalling, depending on the number of percussions and the hardness of the rock. Moreover, the size of the spalled fragments was related to the properties of the WC/Co cemented carbide. [19]

One year later, the major influencing parameters on the wear rate, amount of Co binder and the hardness of the cemented carbide, were outlined [20]. Consequently, the compressive strength and the carbide grain size were pointed out as the most important factors [21].

Referring to a study by Larsen-Basse [9], the wear during rock drilling could be categorized into four different mechanisms, where the dominant mechanisms are depending on the drilled rock type, see 1.3.

In [22] the thermal fatigue failure is not only mentioned again, but also outlined as the most significant wear process during rotary mining techniques. Considering only percussive demolition technique, the generation of heat is much lower, hence, the thermal fatigue seems not to be a notable wear mechanism in this case.

A further point, which is described by Blombery et al. [23], is the removal of the Co from the surface due to abrasive particles leading to a decreased fracture toughness in this area,

and thus a removal of tungsten carbide grains by intergranular fracture. Additional investigations of abrasion of WC/Co cemented carbides by quartz abrasives in a three-body test were made by Larsen-Basse [24] in 1979, in which two mechanisms were described: the binder extrusion due to repeated loading of the surface material in friction-generated shear, and the cracking and fragmentation of the carbide grains as a secondary removal mechanism. The similar two mechanisms were described in [9], whereby the simultaneous but significant independent occurrence of these was particularly pointed out.

Perrott [25] made a slightly different approach, compared to Larsen-Basse [9], classifying the different wear mechanisms of WC/Co cemented carbides into five categories:

1. Scratching abrasion
2. Grinding abrasion
3. Hot abrasion
4. Thermal fatigue
5. Surface spalling

Regarding scratching abrasion, the worn surface exhibit mainly flat areas with some spall craters due to intergranular fracture propagating, usually with a depth of one to two carbide grain sizes, beneath the surface. The carbide grains are crushed or single ones are removed completely, respectively. In grinding abrasion, the WC grains are exposed to extensive fracture due to a preceding larger binder extrusion. Moreover, in some instances exposed carbide grain edges are rounded. Hot abrasion appears when large loads and high drilling velocities occur, leading to a glassy surface with very fine WC fragments. Thermal fatigue starts with instantly initiated fine parallel surface cracks, perpendicular to the sliding direction of the button, developing into the so-called reptile skin. The last proposed mechanism of WC/Co cemented carbides is surface spalling, mainly occurring in percussive drilling. However, this mechanism shows a worn surface with great craters, especially pronounced at higher impact energy and higher rock hardness. [25]

In 2008, Beste and Jacobson [3] presented a novel view of the wear of WC/Co cemented carbides used as drill buttons in rock drilling applications, presenting five classes of possible deterioration mechanisms:

1. Rock cover formation, rock intermixing and rock penetration
2. Embrittlement and degradation of the binder phase
3. Composite-scale crack formation
4. WC grain-scale crack formation
5. Oxidation and corrosion of WC grains

The phenomena occurring in Class 1 have already been described in other studies [4] [26], clearly showing that rock fragments build a solid layer on the cemented carbide parts and even penetrate the material, forming channels between the carbide grains. Usually the crushed rock material covers small local parts of the surface, but nevertheless the mixture of it, together with WC and Co, is then the actual layer interacting with the rock, influencing the wear rate of the drill button [3].

Due to percussive load and a rough contact against the rock, the binder phase gets plastically deformed, further on embrittlement and degradation of the binder is occurring [3]. Consequently, the major part of the initial fcc-Co is transformed to the brittle hcp-Co, causing the mechanical properties of the WC/Co cemented carbide to change [3]. With a mechanical pressure cycling test by Beste et al. [27], the effects on the properties of the cemented carbides caused by this phase transformation were described. Important to note was a decreasing fracture toughness, thermal shock resistance and erosion resistance, though no changes in micro and nano hardness.

Within Class 3 of the presented deterioration mechanisms of WC/Co cemented carbides, the composite-scale crack formation, the incidence of the so-called reptile skin and intergranular cracking are included [3]. This surface damage mechanism is quite commonly detected at drill buttons [12], named after its resemblance to the back of a crocodile. Besides the fact that the exact mechanism behind the formation of the reptile skin is still vague, these crack patterns are not a major problem, unless it is the cause for catastrophic fracture [3].

WC grain-scale crack formation is especially dominant when drilling rocks with high hardness, where local fracture and cracking in individual near-surface WC grains can be observed.

The last deterioration mechanism is the oxidation and corrosion of WC grains, in which a tungsten oxide layer consisting of small, loose attached rounded particles can be observed at times. These particles are built immediately after one percussive hit on the rock and generally get removed with the following contact. [3]

Moreover, Beste and Jacobson [3] described five important mechanisms of material removal (illustrated in Figure 9):

1. Crushing of WC grains and release of fragments (also referred to as impact spalling, impact-fatigue spalling, micro-spalling, grain spalling, grain fracture or grain crushing)
2. Detachment of whole or parts of WC grains
3. Crushing and removal of binder/rock mixture
4. Tribochemical wear of the carbides
5. Detachment of composite scale fragments

The first mentioned removal mechanism is probably the most important, in contrast to the infrequent detachment of whole or parts of WC grains. Removal mechanism number 3 is more or less replacing the earlier assumptions, where the abrasive removal of the Co by its extrusion from the bulk to the surface, is described as a major degradation mechanism [9], [28]. The study by Beste and Jacobson [3] pointed out that this is very rare, however, rock intermixing with the surface of the cemented carbide seems to play an important role during application. Therefore, embrittlement of the binder takes place, followed by crushing fragments of this composite layer. Material removal mechanism number 4 is described by gradual corrosion or oxidation of the surface, where the newly formed layer is mechanically removed. Regarding the last removal mechanisms, it should be mentioned that the detachment of composite scale fragments is usually a rather uncommon event.

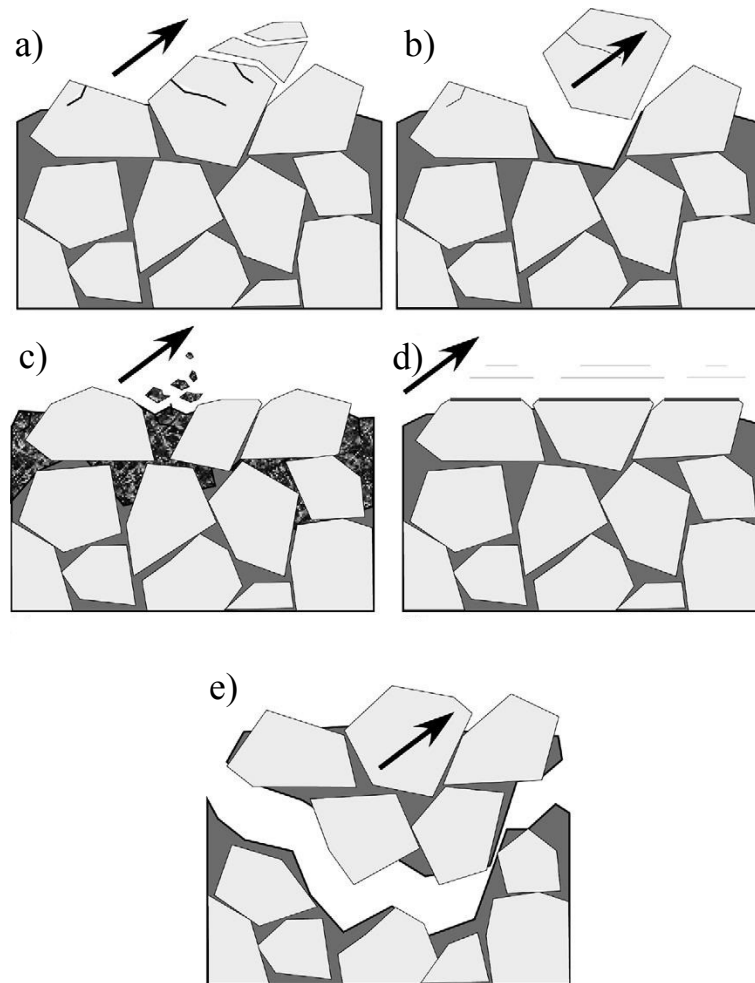


Figure 9: Schematic illustration of five important mechanisms of material removal of rock drill buttons. (a) Crushing of WC grains and release of fragments. (b) Detachment of whole or parts of WC grains (c) Crushing and removal of binder/rock mixture (d) Tribochemical wear of the carbides (e) Detachment of composite scale fragments [3].

2.2 Concrete

In this work, the HILTI bushing tools have been tested in a test rig using concrete C50/60 GK32 as base material.

The composite material concrete is one of the most used construction material on our planet, extremely durable and used more than any other artificial material in the world [29].

It is composed of three different components, namely cement, aggregates, and water. Nowadays concrete is commonly described as a composite material composed of fluid cement paste, usually a lime-based cement with water, and fine and coarse aggregates, typically sand, gravel and crushed stones.

The variety of produced concrete is huge, for instance, the densities range from 160 kg/m³ to 4800 kg/m³ and the compressive strengths from 0.35 MPa up to 275 MPa [30].

Quite often different concretes are classified based on their compressive strength, either tested on cylindrical samples with a diameter of 150 mm and a length of 300 mm ($f_{ck,cyl}$) or cubes with an edge length of 150 mm ($f_{ck,cube}$) and an age of 28 days. Hence, the classification name is made up of the letter C (representing concrete) followed by the compressive strength values of the cylinder test and the cube test given in N/mm^2 , for example C40/50. [31]

2.3 Granite

For the tests executed by the automated test rig a granite was used as base material, mainly due to a higher homogeneity in contrast to concrete.

The igneous rock type granite contains basically 20 – 40 % quartz, potassium and plagioclase feldspar, as well as mica [32]. Regarding the chemical composition silicon dioxide and aluminum oxide are the main part, in detail shown in Table 1.

The properties of granite, as it is a natural material, vary of course in between different extraction sites, but even within the same extraction site slight disparities may appear. However, typical values for the density of granite are in the range of $2.54 - 2.66 \text{ g/cm}^3$, with a Mohs Hardness of 5 – 7. The values of the modulus of elasticity are somewhere between 20 and 60 GPa, in addition the compressive strength ranges between 96.5 and 310 MPa. [18]

Table 1: Average of the chemical composition of granite [33]

SiO ₂	72.04	%
Al ₂ O ₃	14.42	%
K ₂ O	4.12	%
Na ₂ O	3.69	%
CaO	1.82	%
FeO	1.68	%
Fe ₂ O ₃	1.22	%
MgO	0.71	%
TiO ₂	0.30	%
P ₂ O ₅	0.12	%
MnO	0.05	%

3 Testing Methods

Regarding the inserts of demolition tools, such as drill bits or chisels, manual field testing is very time and human resource consuming. However, in addition to the inhomogeneous base material, the individual way of operation by the user could cause inconsistent results. On the other hand, the usage of laboratory tests for simulating the same conditions for the tools as in real application is just as difficult. In this work, different shaped samples and materials have been tested by selected test methods to compare alternative materials for demolition applications in terms of their wear behavior.

3.1 Fracture Toughness Measurement

A major issue, when it comes to the determination of the fracture toughness of cemented carbides is the measurement method. Because it is not able to precrack these materials by fatigue, the fracture toughness cannot be measured in accordance with the recommended British (BS 54479) or American (ASTM E 399-78) standard test methods, therefore a considerable number of alternative methods have been developed [10]. Different methods to measure the fracture toughness are described in [34]. The most widespread method to determine the fracture toughness, especially for qualitative comparison, is the so-called Palmqvist method [35], where a Vickers tip is indented into the surface of the cemented carbide with a load of usually 30 kilogram-force. Due to the relatively high load, cracks occur at the corners of the indent; their lengths are measured (see Figure 10a), and from which the toughness can be calculated.

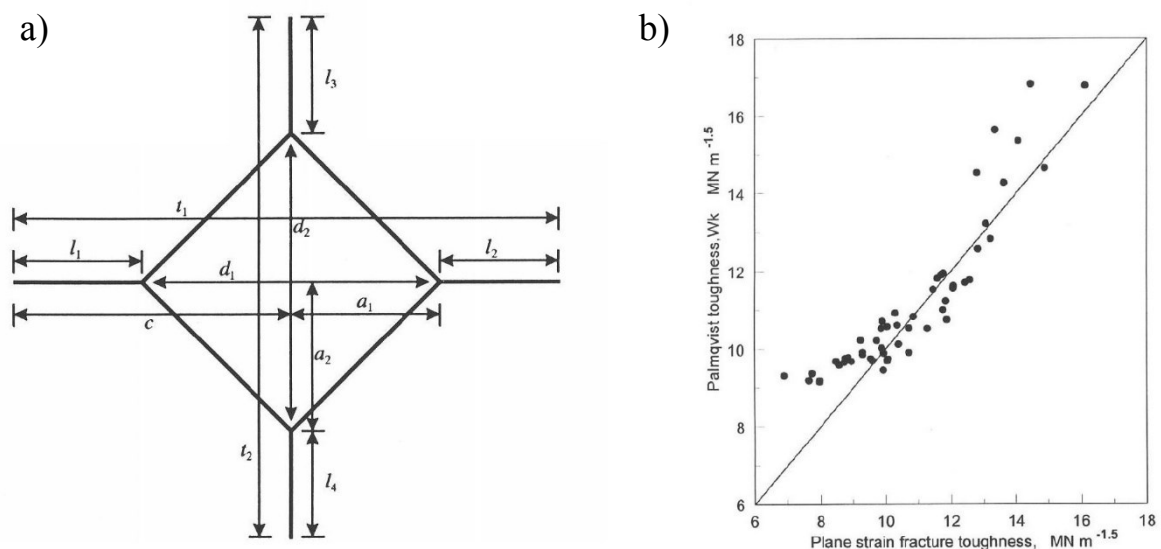


Figure 10: a) Schematic diagram and definitions for the Palmqvist method. b) Comparison of Palmqvist toughness values with plane strain fracture toughness K_{Ic} [35].

In the first step of the determination of the Palmqvist fracture toughness, the so-called Palmqvist toughness W_G is calculated:

$$W_G = \frac{P}{T} \quad (\text{N mm}^{-1}) \quad (1)$$

where P is the load in N and T is the total crack length (sum of all four cracks $l_1 - l_2$) in mm. In the next step, the Palmqvist fracture toughness can be calculated:

$$W_K = A \sqrt{HV} \sqrt{W_G} \quad (\text{MN m}^{-3/2}) \quad (2)$$

where A is an empirical constant of value 0.0028 and HV is the Vickers hardness in Nmm^{-2} . The value W_K can be referred to the plane strain fracture toughness K_{Ic} (shown in Figure 10b). [35]

Due to the variations of the tungsten carbide grain size and the amount of cobalt binder, a wide range of the fracture toughness values of WC/Co cemented carbides can be observed, typical values for cemented carbides range from 5 to 26 $\text{MPam}^{1/2}$ [15].

3.2 Edge Toughness Test

For many brittle materials, the edge chipping is one of the most common reasons for failure, and this is also the case for WC/Co cemented carbides. To examine this behavior of brittle edges under mechanical loading, Almond and McCormick [36] suggested a method in 1986, where a Rockwell-C indenter penetrated a point near the surface of the sample with increasing load until flaking occurred. In this way, the resistance of a brittle material against edge chipping, which correlates with the critical strain energy, can be determined, also referred to as edge toughness. [37] In 2010 the standard DIN CES/TE 843-9 was published, where the method of test for edge-chip resistance of ceramics is described. The setup of the edge toughness test is shown in Figure 11.

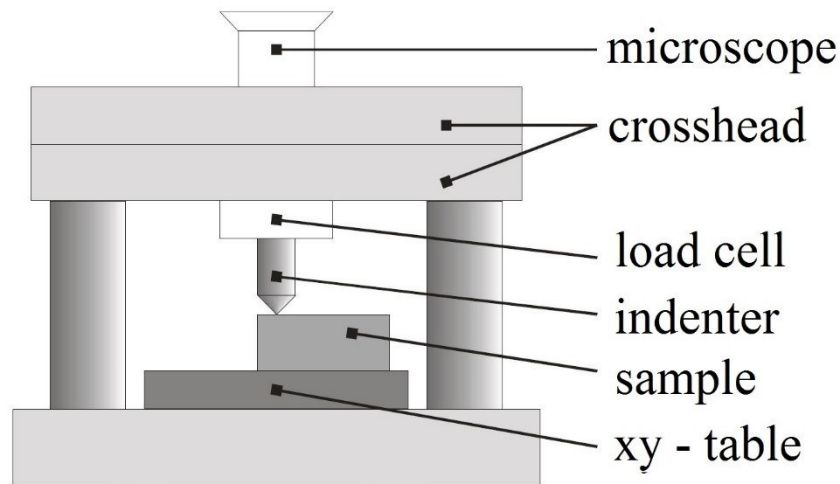


Figure 11: Edge toughness testing machine [37].

There are two different ways to perform this test. The first way is to maintain the exact same distance from the edge for every test and calculate the average edge toughness. Alternatively, the distance can be increased or decreased and the load values plotted against the distance, and hence the slope of the regression line is the edge toughness. A schematic illustration of an edge sample before and after testing is shown in Figure 12.

In case of fixed experimental conditions, for example indenter shape and edge geometry, a linear relationship between the peak load P and the distance from the sample edge d is recognized. This is described by:

$$P = P_0 + M \cdot d \quad (3)$$

The slope M is characteristic for each material, in case of the same testing conditions. Contrary to expectations, the best fit line usually does not go through the origin, hence, there seems to be an infinite load P_0 required to cause a chip exactly at the edge. Explanations could be, for instance, uncertainties during the measurement [36] or internal stresses in the material. However, for sharp edges this deviation is very small, thus formula (3) can be written as:

$$P \approx M \cdot d \quad (4)$$

Due to this approach, it is vital that all tests are performed near the edge, if this is the case, the slope M is representing the edge toughness of the tested material. [36]

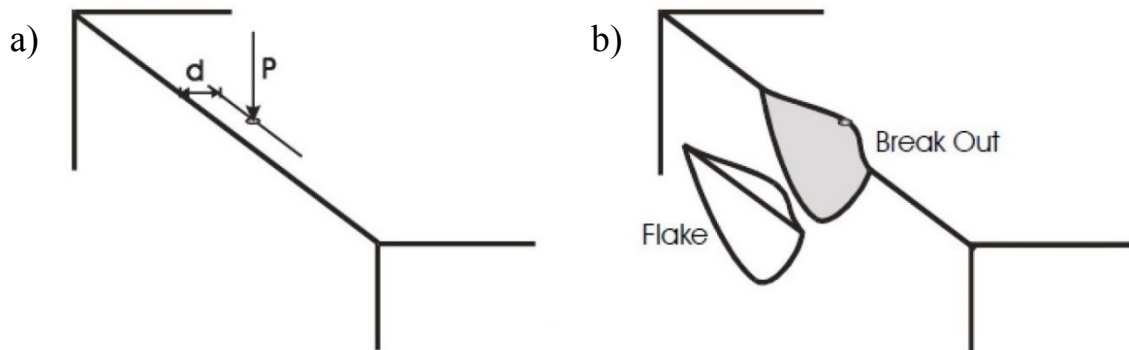


Figure 12: Schematic drawing where distance from the edge of the loading point is pictured a) before, and b) after the test [37].

3.3 LCPC Test

In terms of finding a laboratory-scale test to imitate the mechanical loading of a cemented carbide pin of a HILTI bushing tool in real application as closely as possible, the so-called LCPC test [38] was attempted.

The LCPC Abrasivity test was developed by the “Laboratoire Central des Ponts et Chaussées” in 1986, by which the LCPC Abrasivity Coefficient can be determined and used as a measurement of the abrasivity of the material. The test procedure and testing device is described in the French Standard P18-579, established 1990. Basically, there is a 750 W motor rotating a metal impeller (steel plate, 50 x 25 x 5 mm) in a cylindrical container filled with the granular sample ($500 \text{ g} \pm 2 \text{ g}$), the testing aperture is shown in Figure 13. Due to the mass loss of the impeller during each test, which usually takes 5 minutes, the abrasivity of the sample can be determined.

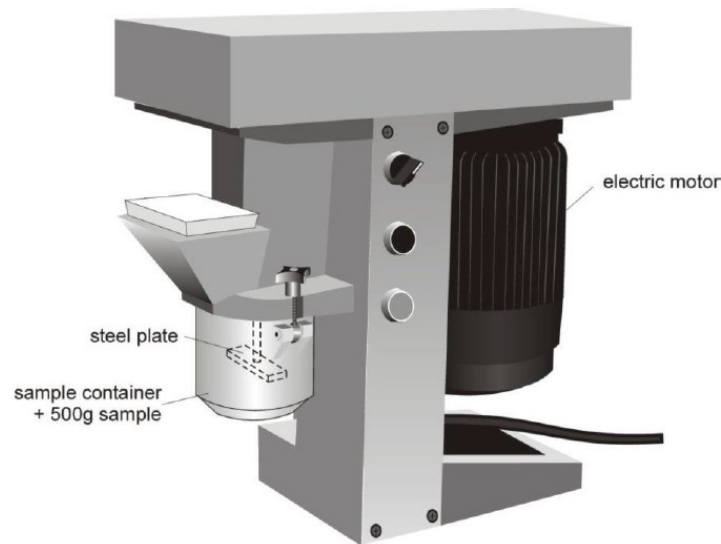


Figure 13: Testing aperture for the LCPC Abrasivity test [39].

Based on the principle of the French Standard P18-579 [38], in the current work the impeller was modified so that two cemented carbide samples can be positioned on it (see Figure 14). The clamping plate is attached with a screw on the side of the steel plate, and thus fixing the cemented carbide sample. The weight of each sample is measured before and after every single test (5 min), hence, using the density of the material, the volume difference can be calculated.

In a study of the wear of cemented tungsten carbide percussive drill-bit inserts the same concept with slightly different construction of the modified impeller was used [40].

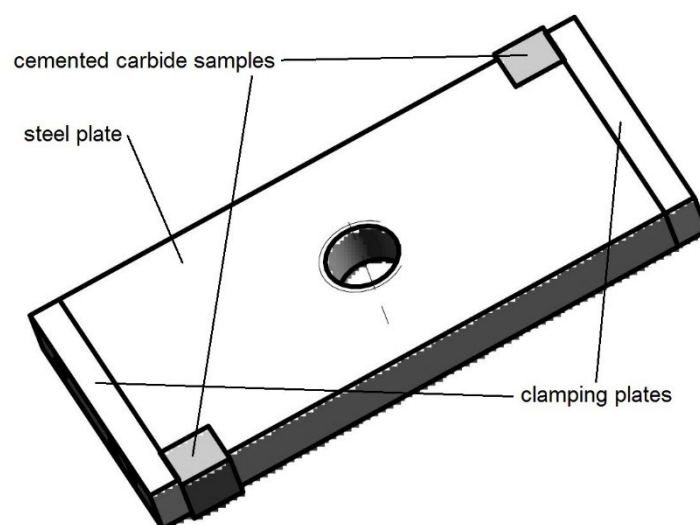


Figure 14: Modified impeller for testing cemented carbide samples by the LCPC Abrasivity test.

3.4 Application Testing

The investigated cemented carbide pins of the serial and modified bushing tools have been tested in a fully-automated 3 axis test rig (see Figure 15) at HILTI AG Headquarters in Schaan / FL. The HILTI TE 70-ATC7AVR combi-hammer was used, with a max hammering frequency of 2760 impacts per minute and a single impact energy of 11.5 J [41].

This setting enables the possibility to test different tools on various base materials with real-life machines, revealing close to real conditions in a fully automated way.

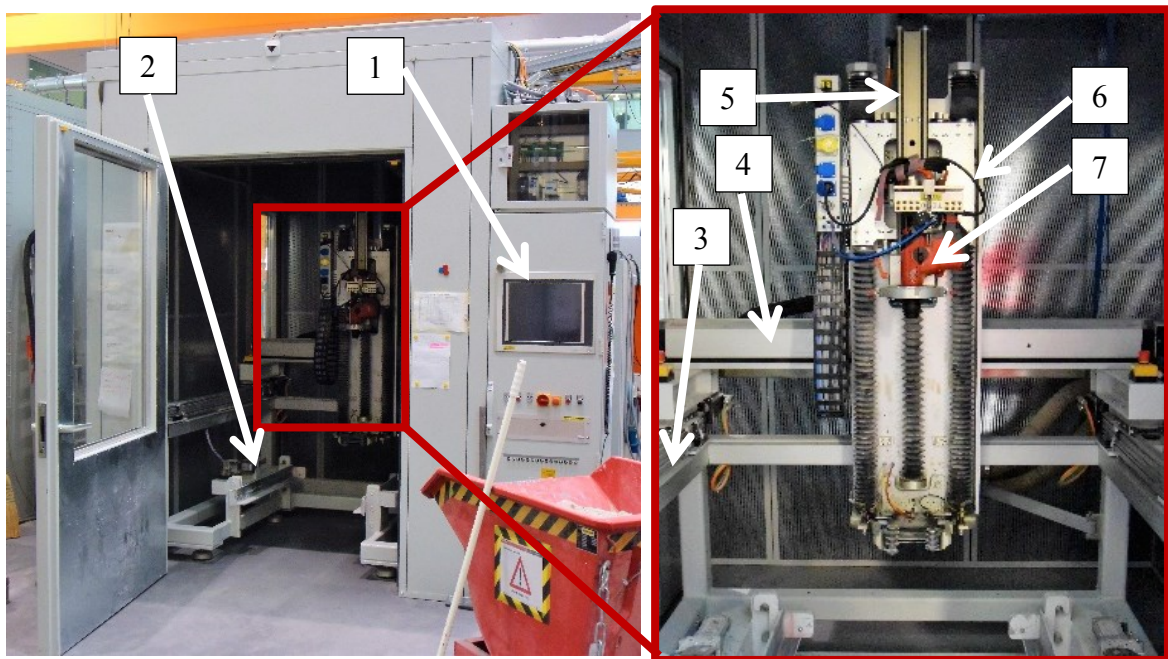


Figure 15: Fully automated 3-axis test bench situated at HILTI AG Headquarters in Schaan, FL. A combi-hammer tool is already installed, to start the test program a specific chisel and base material must be inserted in the next steps.

- 1) Control panel
- 2) Fixation for base material
- 3) X-stage
- 4) Y-stage
- 5) Z-stage
- 6) Fixation for machine
- 7) Inserted HILTI TE 70-ATC7AVR combi-hammer

4 Analysis Methods

When it comes to the analysis of wear, a wide range of scales needs to be covered. Beginning with the macroscopic change of a certain shape of the investigated part, which may imply if it is, for example, a gradual wear behavior or unevenly distributed, all the way down to the microscopic scale, where a specific wear mechanism can be observed, for example intergranular cracking of a single tungsten carbide grain. Due to this, the analysis of the wear of alternative WC/Co cemented carbides for demolition applications, investigated in this work, was categorized into the macroscopic and the microscopic part.

It must also be mentioned here that, despite of highly developed analysis instruments and advanced measurement technologies, the analysis of wear behavior or rather wear mechanisms are nearly solely possible by subjective analysis. A reliable approach was done by Mosely et al. [42], where the intensity of the wear was ranked between 0 and 3 by a subjective measurement based on an evaluation of Scanning Electron Microscope (SEM) images, examples shown in Figure 16.

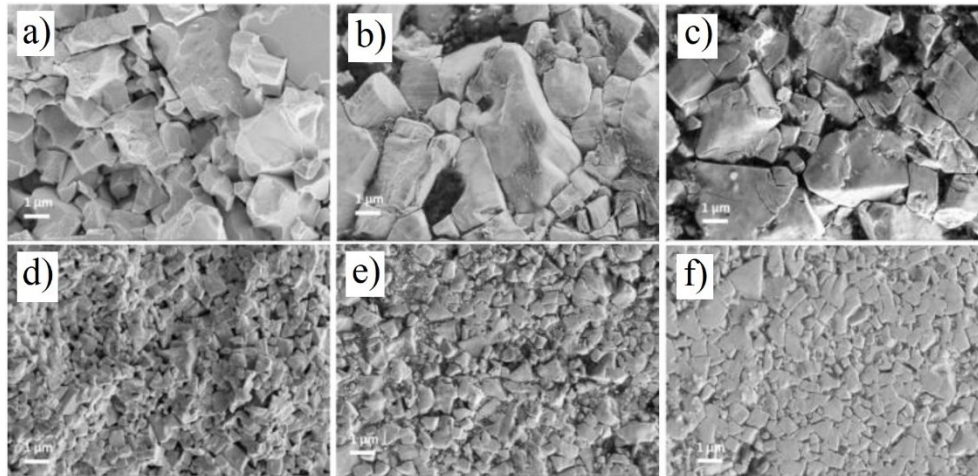


Figure 16: Wear intensity assessment reference pictures, the upper images represent a coarse grained cemented carbide, the lower a fine grained. a) fatigue/abrasion intensity "0", b) fatigue intensity "1", c) fatigue intensity "3", d) fatigue/abrasion intensity "0", e) abrasion intensity "1.5", f) abrasion intensity "3" [42].

4.1 Macroscopic Analysis Methods

It is well known that in fractography it is vital to not just concentrate on the details, but to step back and to have a look at the overall appearance of the investigated part. Like fracture, wear is also a mechanical failure mode, hence, to analyze the situation of a worn WC/Co part from a macroscopic point of view is equally important to define the wear mechanisms.

A quite common and easy way to determine differences concerning wear behavior of different samples and materials is using weight measurement, for example before and after a certain test. Accordingly, the volume difference can be calculated by means of the density of the specific material, further, this can be used to rank different samples in terms of their wear behavior.

Furthermore, the identification of geometrical changes of the tested samples may be a simple finding and a point of not inconsiderable importance. The difference of the shape before and after a test, or the variance of certain dimensions, could give information about the uniformity of the wear, or point out discrepancies.

To verify and to visualize the above-mentioned points, the optical 3D measurement device “Alicona™ InfiniteFocus” was used (see Figure 17).



Figure 17: a) Alicona™ measurement equipment, Visualization of a b) unworn and c) worn WC/Co cemented carbide pin of a HILTI bushing tool.

4.2 Microscopic Analysis Methods

On the microscopic scale, Light Optical Microscopy is the dominating method to investigate the material surface, such as the surface of a worn sample.

With the help of visible light and a system of lenses, the light optical microscope can magnify images of small dimensions. There are numerous different techniques, for example polarized, phase contrast and bright/dark field illumination. Nowadays, the microscope is directly connected with a CCD camera showing the resulting image directly on the computer screen. Within this work, the light optical microscope was used to analyze worn WC/Co cemented carbide samples after different test methods.

Based on the mentioned limitation of the maximal resolution, the SEM is the next step to analyze and characterize material surfaces.

The principle of the SEM is the acceleration of electrons through a voltage difference between cathode and anode, with values between 0.1 keV and 50 keV, towards the specimen. This emitted primary electron beam is focused onto the surface, causing different responses of the material which can be detected (shown in Figure 18). Basically, the obtained information of a SEM investigation is built upon the detection of the secondary electrons (SE), the backscattered electrons (BSE) and the characteristic X-ray radiation. [43]

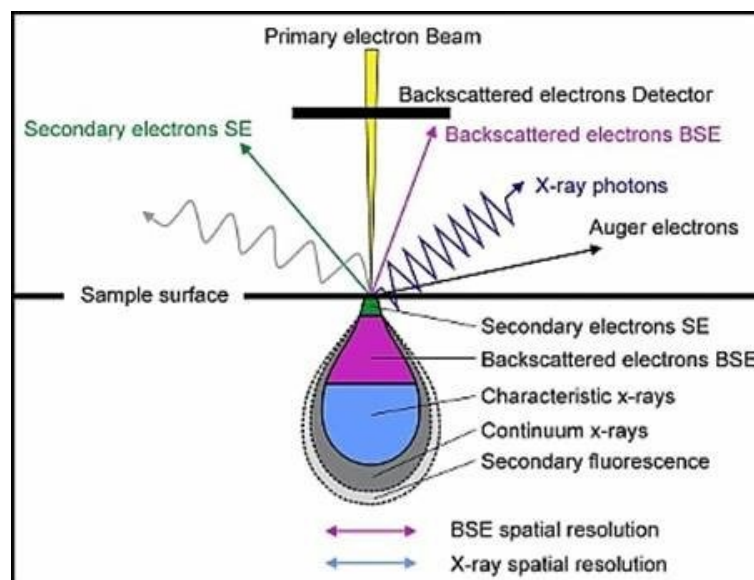


Figure 18: Interactions between the primary electron beam and the investigated sample surface [44].

5 Results and Discussion

Due to its nature, WC/Co cemented carbides reveal a very broad range of material properties, such as hardness and fracture toughness, depending on the composition of this composite material. Therefore, for the investigation of the wear mechanisms a selection of different WC/Co grades has been used (shown in Table 2). To begin with, two categories were defined based on two different suppliers for the samples, with slightly different production parameters. Furthermore, within each group the WC/Co samples have a different amount of Co binder content and / or a varied mean grain size of the tungsten carbide grains. In comparison to B1-6Co, the grade B2-6Co contains different grain growth inhibitors. Although the availability of WC/Co cemented carbide samples with suitable shapes and sizes was restricted, this selection offers a wide range of commonly used materials within demolition applications. The Figure 19 and Figure 20 show the microstructure of the different grades, captured with a Leica DM6000M light optical microscope and a magnification of 100 x. At this point it should be mentioned that for the finer grain sizes the light optical microscope comes to its limit.

Table 2: Selected specifications of investigated WC/Co cemented carbide grains.

Grade designation	Grain Size (according to supplier)	Co content [m%]	Density [kg/m ³]	Vickers Hardness [HV10]
A1-6Co	medium	6.0	14950	1430
A2-8Co	medium	8.0	14750	1310
A3-8.5Co	medium	8.5	14650	1420
A4-10Co	extra-coarse	10.0	14600	1130
A5-11Co	medium	11.0	14500	1260
B1-6Co	fine	6.0	14900	1400
B2-6Co	fine	6.0	14900	1430
B3-6Co	coarse	6.0	14900	1180
B4-9.5Co	fine	9.5	14550	1300
B5-9.5Co	coarse	9.5	14550	1020

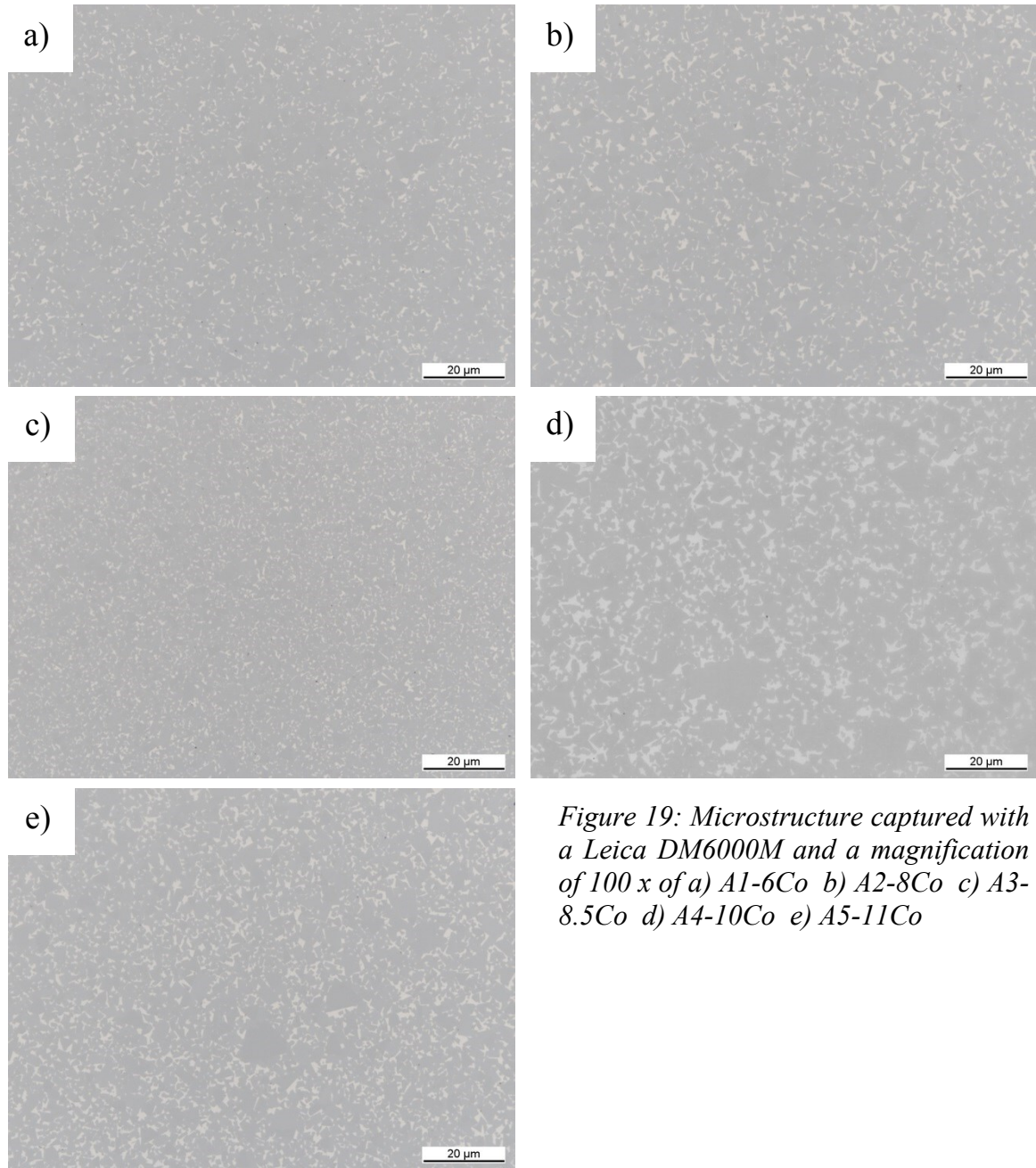


Figure 19: Microstructure captured with a Leica DM6000M and a magnification of 100 x of a) Al-6Co b) Al-8Co c) Al-8.5Co d) Al-10Co e) Al-11Co

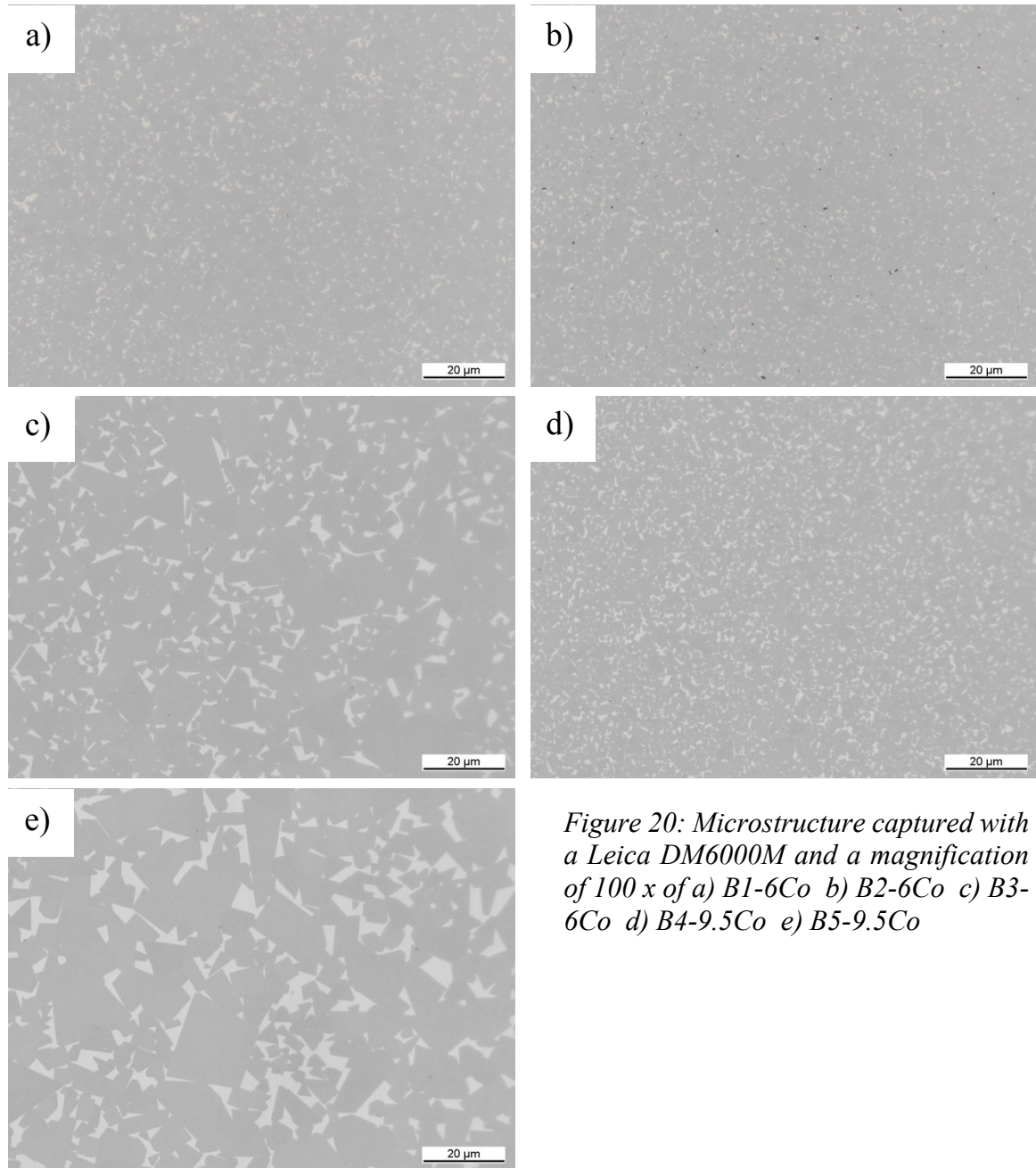


Figure 20: Microstructure captured with a Leica DM6000M and a magnification of 100 x of a) B1-6Co b) B2-6Co c) B3-6Co d) B4-9.5Co e) B5-9.5Co

5.1 Grain Size Distribution

For determining the average grain size of the investigated cemented carbide grades the lineal intercept procedure, described in the ASTM standard E112-12 [45], was used. As defined in the standard, the minimum number of intersections was 50 and the determination was based on light optical microscope images with a magnification of 100x. The results are shown in Figure 21 and Figure 22, where the vertical axis represents the cumulative distribution and the horizontal axis shows the grain sizes in the logarithmic display.

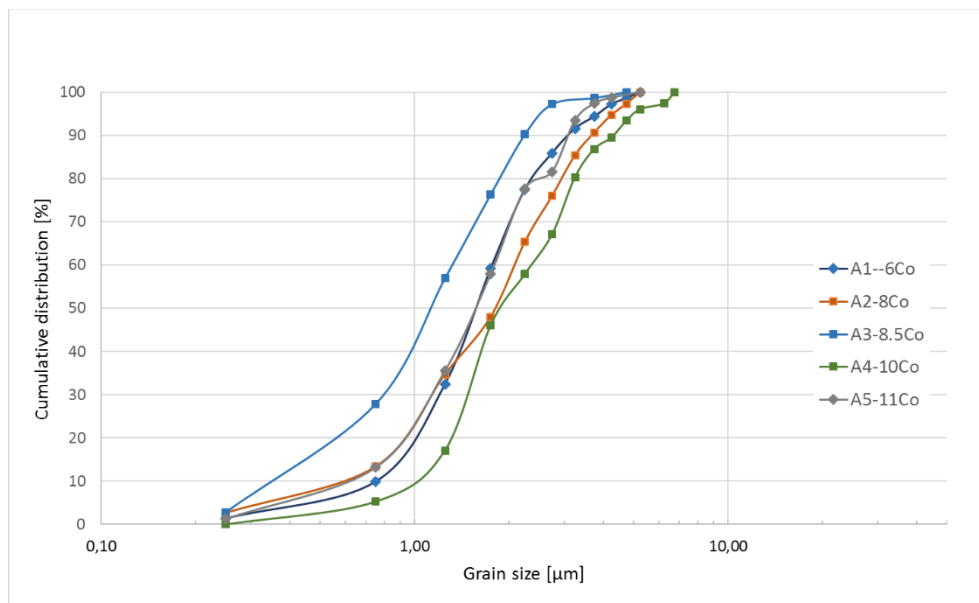


Figure 21: Grain size distribution for the A-grades cemented carbides.

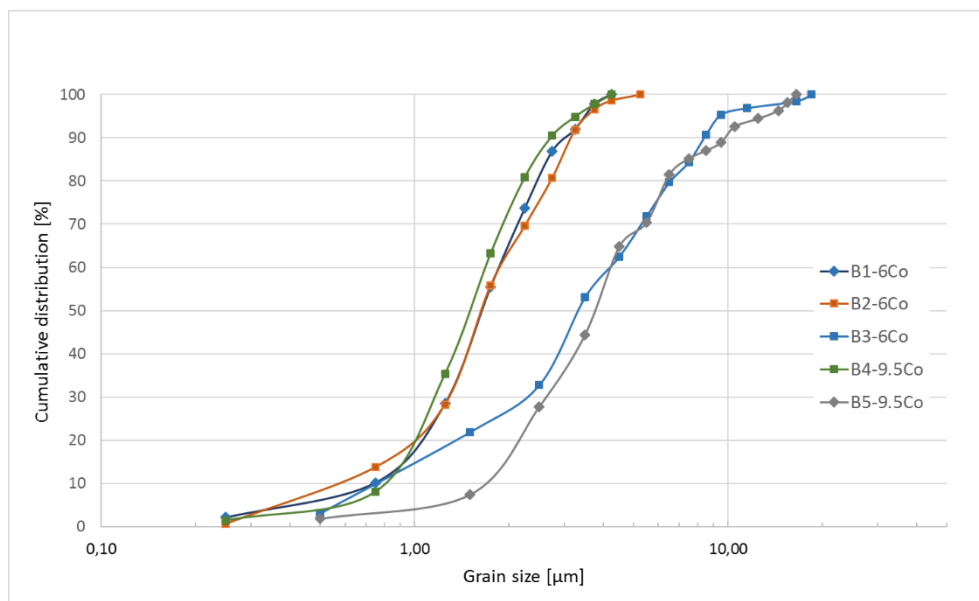


Figure 22: Grain size distribution for the B-grades cemented carbides.

An overview of the average grain size of the different material grades is given in Table 3.

Table 3: Average grain size of investigated WC/Co cemented carbide determined by the lineal intercept procedure according to [45].

Grade designation	Grain size according to supplier [μm]	Measured average grain size [μm]
A1-6Co	1.3 – 2.5	2.0 ± 0.2
A2-8Co	1.3 – 2.5	2.2 ± 0.2
A3-8.5Co	1.3 – 2.5	1.5 ± 0.2
A4-10Co	> 6.0	2.6 ± 0.2
A5-11Co	1.3 – 2.5	2.0 ± 0.2
B1-6Co	4.0 -5.0	2.0 ± 0.1
B2-6Co	4.0 -5.0	2.1 ± 0.1
B3-6Co	20.0	4.8 ± 0.8
B4-9.5Co	4.0	1.9 ± 0.1
B5-9.5Co	25.0	5.2 ± 0.8

Besides the difficulty of applying the lineal intercept procedure on two phases materials and the limitations of the light optical microscopy the determination of the grain size distributions shows good results. A reason for different average grain sizes for quite similar cemented carbides is the fact, that different suppliers may use slightly different production parameters. The average grain size of the investigated cemented carbide grades mainly varies around 2 μm . The grade A3-8.5Co reveals the finest grain size, and the grades B3-6Co and B5-9.5Co show coarser grain sizes around 5 μm . These measurements also point out the importance of the analysis, irrespective of values from the suppliers, pointed out by looking at the values for grade A4-10Co and B3-6Co.

5.2 Mechanical Properties

The measurement results of selected mechanical values of the investigated cemented carbide grades are given in this section.

5.2.1 Hardness and Palmqvist Fracture Toughness

The hardness HV30 of the different material grades was measured with a LECO V-100-C hardness tester. The results are shown in Table 4.

The fracture toughness was determined with the Palmqvist method, for this the hardness tester LECO V-100-C with a load of 30 kg was used. Table 4 gives the results of this measurement.

There are no results for the fracture toughness of the cemented carbide grades with high binder content and/or coarse grain size, due to the limitations of the Palmqvist method, more precisely the occurrence of multiple cracks at the corners of the hardness measurement indent.

Table 4: Results of the hardness measurements and Palmqvist fracture toughness determination

Grade designation	Hardness [HV30]	Palmqvist fracture toughness [MPa \sqrt{m}]
A1-6Co	1389 \pm 17	10.8 \pm 0.2
A2-8Co	1297 \pm 5	12.4 \pm 0.4
A3-8.5Co	1413 \pm 4	11.6 \pm 0.2
A4-10Co	1164 \pm 6	–
A5-11Co	1205 \pm 22	–
B1-6Co	1409 \pm 3	10.5 \pm 0.2
B2-6Co	1425 \pm 10	11.7 \pm 0.4
B3-6Co	1150 \pm 15	–
B4-9.5Co	1282 \pm 14	14.2 \pm 0.6
B5-9.5Co	987 \pm 14	–

The inverse relation between the measured fracture toughness and hardness, described in 2.1.1 is shown in Figure 23.

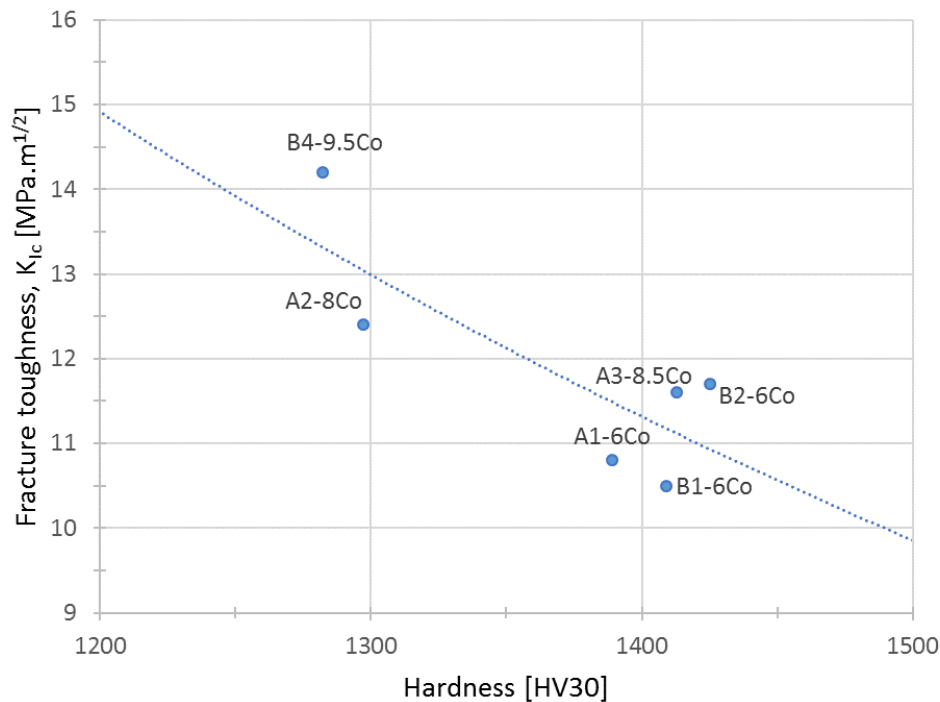


Figure 23: Determined Palmqvist fracture toughness over measured hardness values.

5.2.2 Edge Toughness

The edge toughness tests in this work were performed at the “Lehrstuhl für Struktur- und Funktionskeramik” at the Montanuniversitaet Leoben, where the testing device “Engineering Systems (NOTTM) ET500” was used (see Figure 24).

The measuring principle was explained in Section 3.2. The testing speed was 0.5 mm/min and all tests were performed at room temperature. Due to the not sufficient accuracy of the microscope on the edge toughness testing device, the exact distance of the loading point from the edge was measured using an Olympus SZH10 stereo microscope after the test. An example of a distance measurement after a test is shown in Figure 25.

The results of the edge toughness tests are given in Table 5, and plotted against the before determined Palmqvist fracture toughness in Figure 26. Due to no valid results for some cemented carbide grades, Figure 26 shows only six out of ten grades.



Figure 24: Edge toughness testing machine ET500

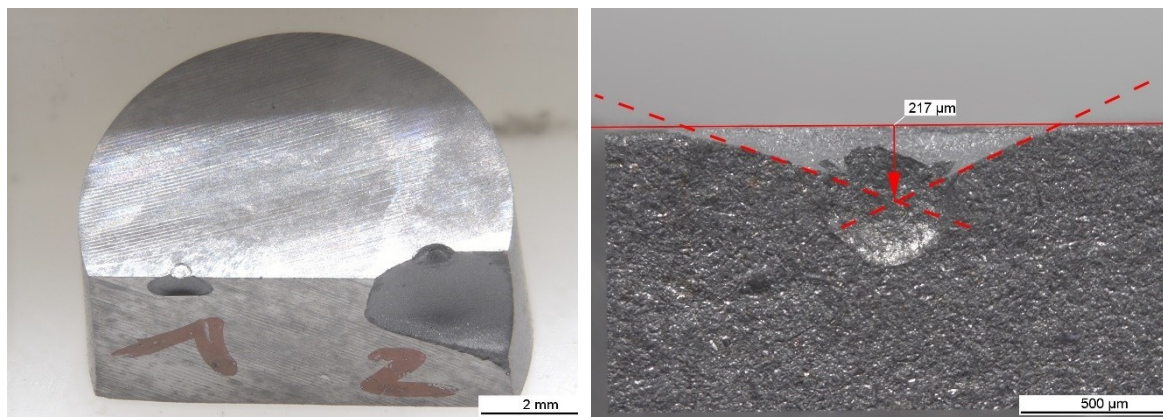


Figure 25: a) A valid result of an edge flake test on the left side of the sample, an invalid on the right. b) An example of the distance measurement of the loading point from the edge of the sample after a test.

Table 5: Results of the edge toughness testing

Grade designation	Edge toughness [N/mm]
A1-6Co	2865 ± 672
A2-8Co	3655 ± 786
A3-8.5Co	3799 ± 636
A4-10Co	3812 ± 642
A5-11Co	2634 ± 944
B1-6Co	2482 ± 690
B2-6Co	2838 ± 554
B3-6Co	3172 ± 634
B4-9.5Co	2548 ± 437
B5-9.5Co	2744 ± 388

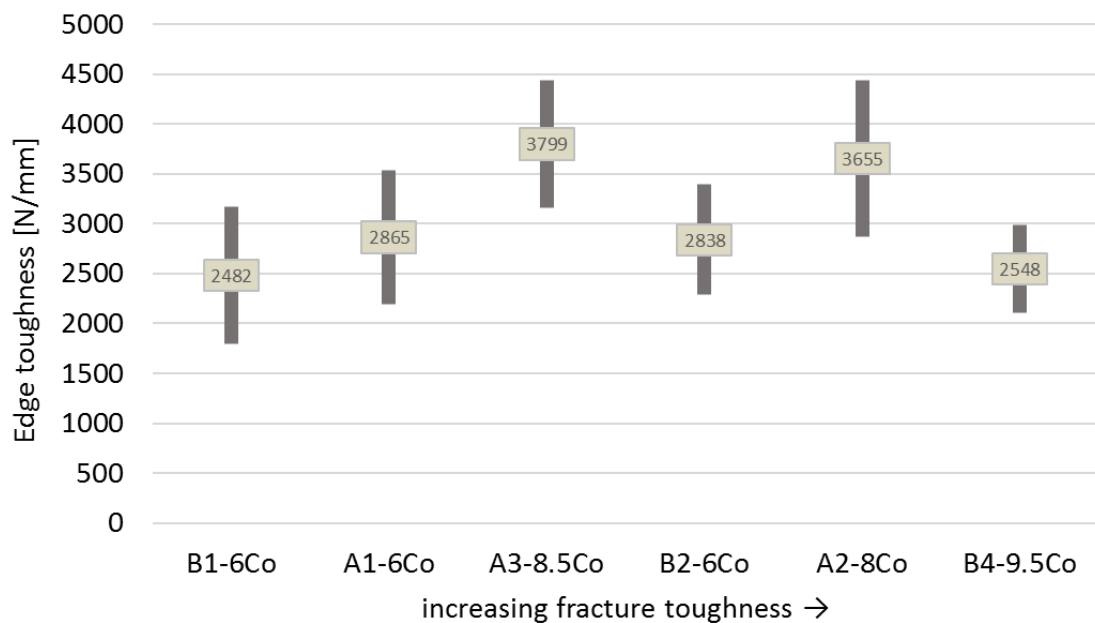


Figure 26: Correlation between the edge toughness and the determined Palmqvist fracture toughness (values see table 4) of the investigated cemented carbide grades.

5.2.3 Discussion of the results

The measured hardness values reveal good correlation to the hardness values from the specification of the different material grades. The measurement of the Palmqvist fracture toughness was more challenging, which basically rests on the measurement method. This issue was already discussed in Section 2.1.1. A proper measurement was not possible, due to multiple cracks at the corners of the hardness indent, for material grades with high binder content (A4-10Co and A5-11Co) and coarse grain sizes (B3-6Co and B5-9.5Co).

A major issue of the edge toughness testing was the manual sample preparation. Due to the manual sample cutting out of small starting samples the exact 90° angle cannot be ensured, additionally the surface of the A-grades (as sintered) and B-grades (cut) were different. That can be also a reason why the correlation between the edge toughness and the Palmqvist fracture toughness (Figure 26) shows no clear trend.

The relation between the fracture toughness (K_{Ic}) and the critical strain energy release rate (G_c) cannot be shown, because the needed values of the moduli of elasticity are not known for the investigated materials.

The scattering of the values is in a quite common range. It could be said, that the investigated material grades are too similar that the edge toughness testing under the previous mentioned conditions reveals a clear correlation.

5.3 LCPC Wear Test

For the LCPC wear tests a testing machine produced by C.E.T.E de l'ouest (Designation: Abroy; Type: 461B; Serial no.: 39) was used (see Figure 27). The principle of the test was explained in Section 3.3. The duration of one test was 5 minutes, for each material 4 tests have been done. The abrasive medium used was “Rötz” gravel 4/11 mm.

The samples (5 x 5 x 4 mm) were prepared by cutting and the surface was grinded and polished. Before and after every test the weight of the cemented carbide samples was measured with a digital scale of the type “Sartorius A120S”.

The results of the LCPC wear test for each material grade group are shown in Figure 28 and Figure 29, where the volume difference for each material is plotted over the testing time.



Figure 27: LCPC testing machine C.E.T.E de l'ouest, Abroy, Type 461B, No.: 39.

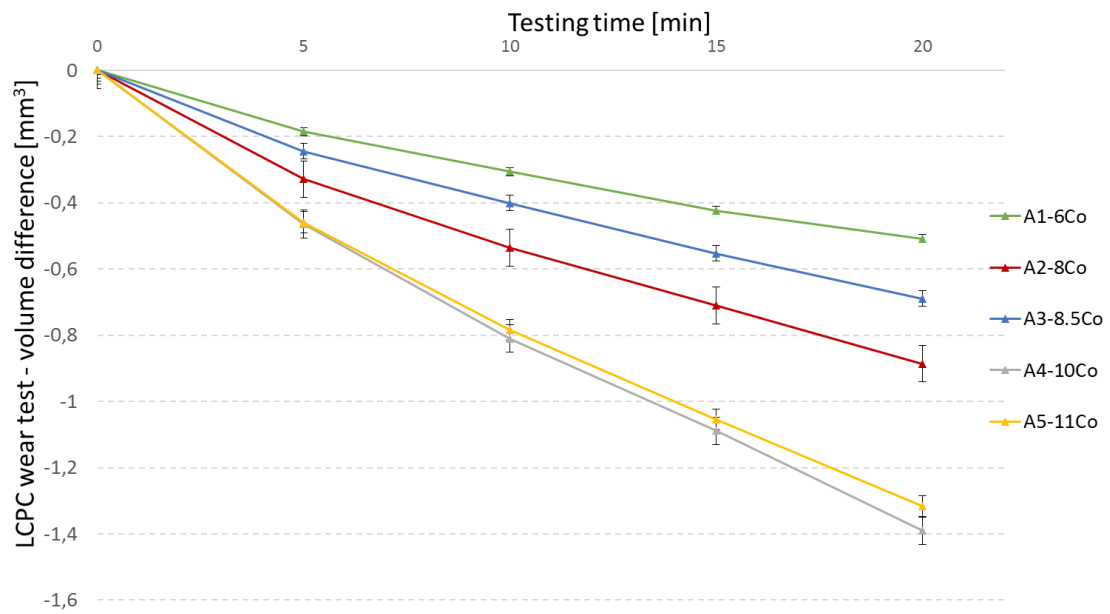


Figure 28: A-grades results of the LCPC wear test.

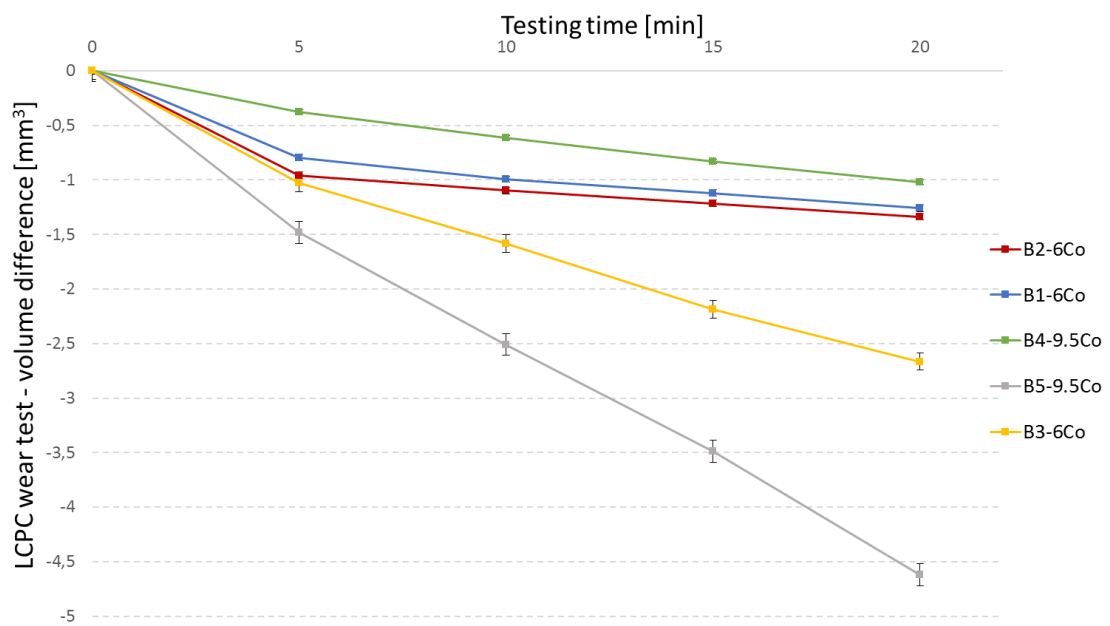


Figure 29: B-grades results of the LCPC wear test.

5.3.1 Discussion of the results

It is shown that the LCPC wear test is a reasonable possibility to compare different cemented carbide grades regarding their wear rate. Figure 30 reveals a clear correlation to the hardness of the tested material grades, where the volume difference increases with decreasing hardness. The hardest grades A1-6Co and B2-6Co (1430HV10) show the lowest volume difference, while the grade with the lowest hardness B5-9.5Co (1020HV10) has the highest volume difference after 4 tests at 5 minutes.

The testing, as well as the sample preparation, is quite simple and the deviation of the results are small. Even though it was not possible to use new clamping plates and/or a new impeller plate for every test, and the height of the cemented carbide samples was varying due to the manual sample cutting, the variations in the results are insignificant.

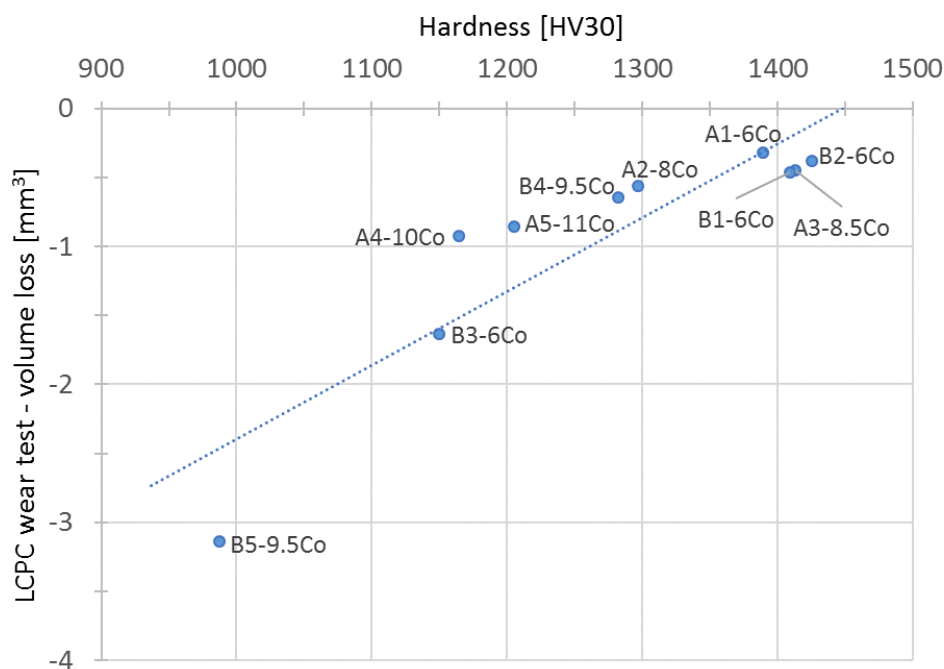


Figure 30: Correlation between the volume loss during the LCPC wear tests and the measured hardness. The volume difference measurement was started at the second test to avoid influences of the starting steel plate.

5.4 Application Testing

The application testing was performed in a fully-automated 3 axis test rig (see Section 3.4). The used combi-hammer, HILTI TE 70-ATC7AVR, has a max hammering frequency of 2760 impacts per minute and a single impact energy of 11.5 J. The base material was the granite type “Herrenholz aus hellem Baywaldgranit” with the dimensions 800/500/200 mm and the surface was sandblasted.

For this testing, only the B-grade cemented carbides have been tested because pin geometries were necessary to build the so-called modified bushing tool, which could be used in the test rig. For the A-grade cemented carbides the pin geometry was not available. The different geometries of the B-grades are shown in Figure 31, for the dimension see Table 6. These pins were brazed into drilled holes of steel heads to create a tool which could be used for the application testing, the so-called modified bushing tool (see Figure 32).

To avoid the contact of the steel head with the base material during chiseling, which leads to increasing temperature and brazing failure, the chiseling depth was adapted to the size of the tested pins. A total chiseling depth of 300 mm was achieved for each grade to ensure the comparability (see Table 6).



Figure 31: The different geometries of the pins for the application testing (from left to right): B2-6Co, B1-6Co, B4-9.5Co, B3-6Co and B5-9.5Co.

Table 6: Dimension of the application tested cemented carbide grades.

Grade designation	Diameter [mm]	Height [mm]	Chiseling depth [mm]
B1-6Co	8.2	11.4	300 mm
B2-6Co	7.4	10.5	300 mm
B3-6Co	11.8	19.0	300 mm
B4-9.5Co	10.4	12.0	300 mm
B5-9.5Co	12.0	21.7	300 mm

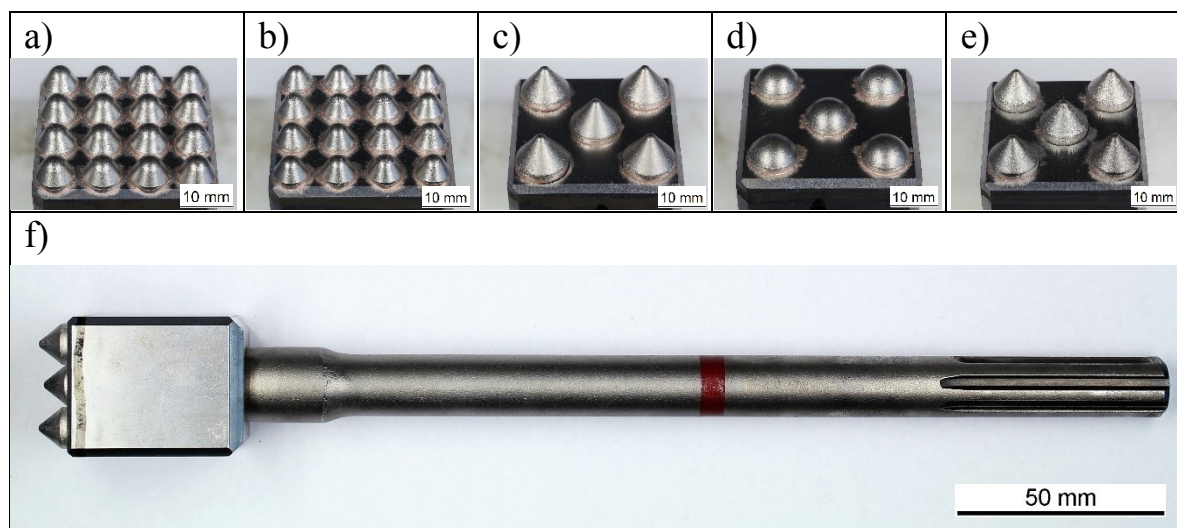


Figure 32: The modified bushing tool heads for the grade a) B1-6Co, b) B2-6Co, c) B3-6Co, d) B4-9.5Co and e) B5-9.5Co. f) shows the whole modified bushing tool for the grade B4-9.5Co.

Before and after the application test, images have been made with a “Leica M205A” stereo microscope and the height of the pins on the steel heads and the angle of their tips was measured with the software “IMS Client”. Furthermore, an optical 3D measurement with the “AliconaTM InfiniteFocus” device was made before and after the test, by which a volume difference measurement with the software “AliconaTM MeasureSuite 5.3.1.” could be made.

The measured volume difference after 300 mm of chiseling is illustrated in Figure 33. The calculated results of the percental height reduction, angle increase and volume difference are shown in Table 7.

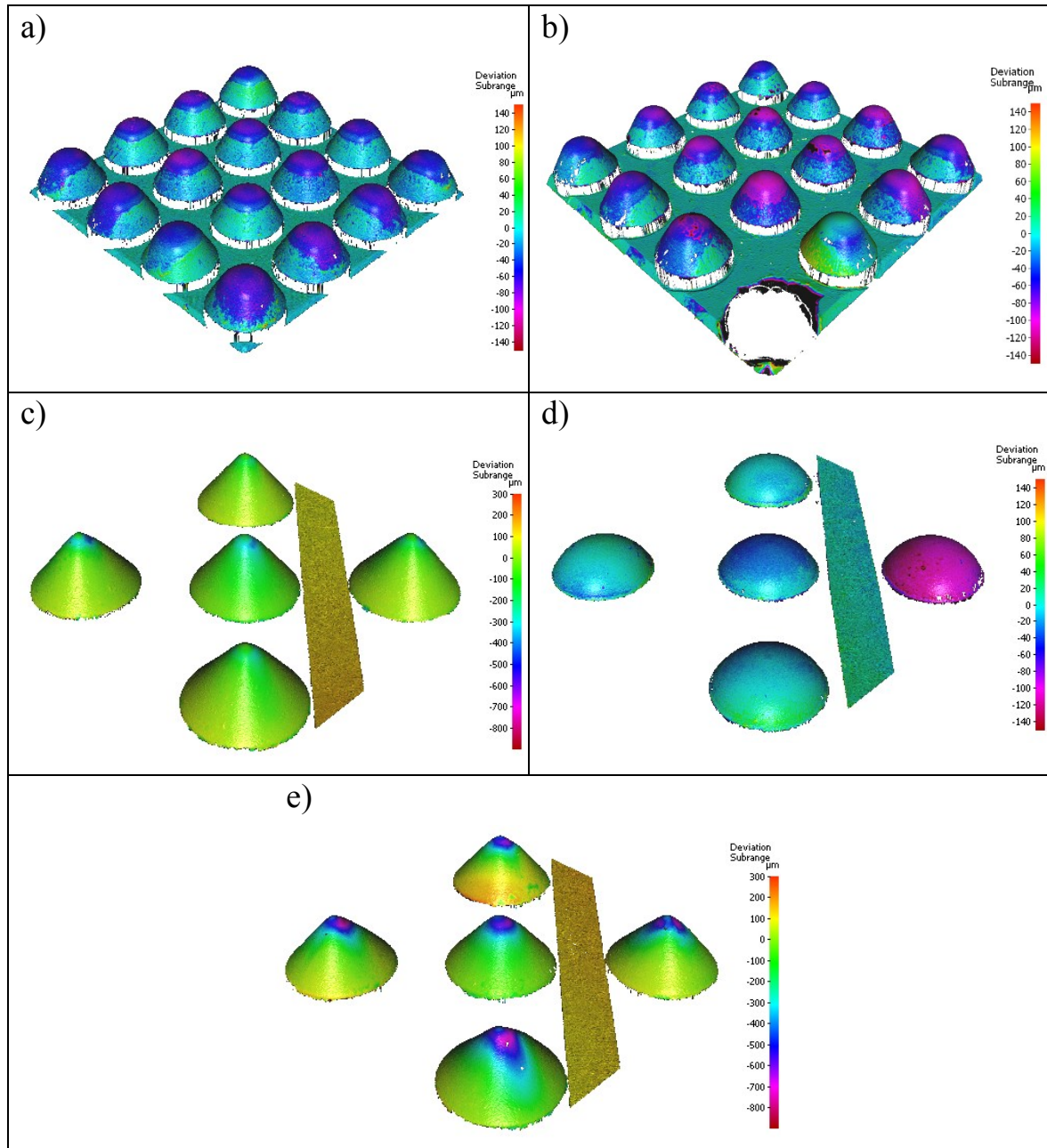


Figure 33: The visualization of the volume difference measurements of the modified bushing tools during application testing (300 mm in granite) for the grade a) B1-6Co, b) B2-6Co, c) B3-6Co, d) B4-9.5Co and e) B5-9.5Co. It should be noted that the scale for the bigger pins (c&e) is different to the scale of the others.

Table 7: The calculated percental differences of the height, angle and volume of the different cemented carbide grades during application testing (300 mm in granite).

Grade designation	Δ Height [%]	Δ Angle [%]	Δ Volume [%]
B1-6Co	-1.21	+0.26	-0.78
B2-6Co	-1.26	+1.09	-1.32
B3-6Co	-2.48	+2.19	-3.54
B4-9.5Co	-1.95	-----	-1.37
B5-9.5Co	-7.75	+6.08	-5.50

The correlation between the volume difference and the grain size of the tested cemented carbide grades is shown in Figure 34.

To compare the volume difference during the application testing with the volume difference during the LCPC wear test, the results are plotted in Figure 35.

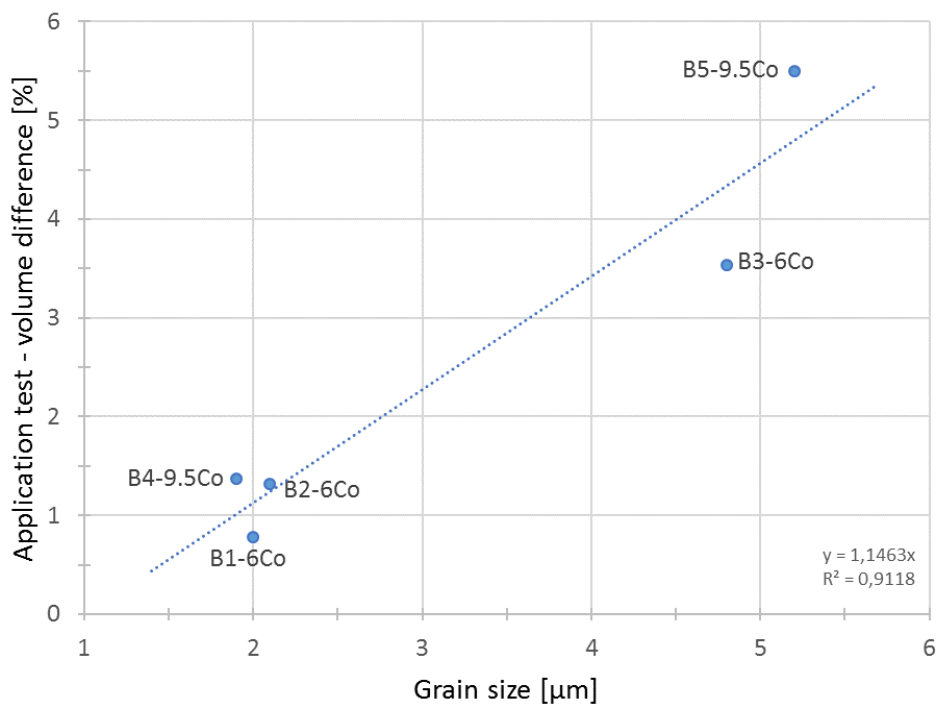


Figure 34 Correlation between the volume difference during the application testing and the grain size of the tested cemented carbide grades.

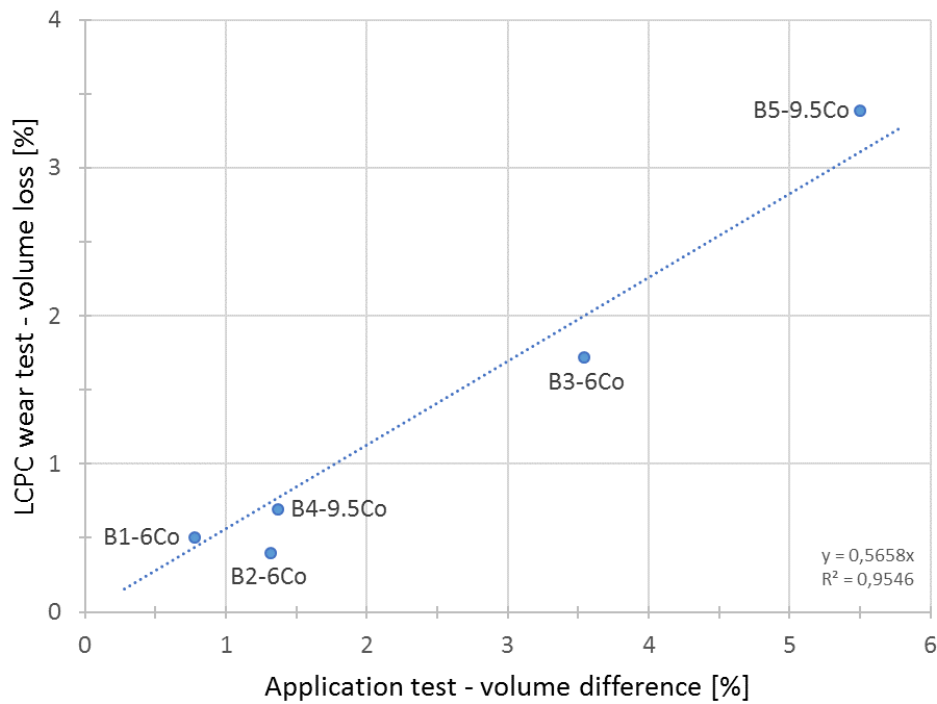


Figure 35: Correlation between the volume difference during the application testing and the LCPC wear test.

Regarding the microscopic analysis, cross-sections of the cemented carbide pins have been cut, grinded and polished after the application testing to identify the wear mechanisms of the different grades and/or geometries (see Figure 36 – Figure 40).

The surface of the tip area (Figure 36a) of the grade B1-6Co shows a relatively smooth overall appearance, without large breakouts. A closer look (Figure 36c) shows mainly rounded tungsten carbide grains (1) along the surface. A few cracks in the carbide grains (2) and some crushed grains (3) can be seen, but these are minor effects. A look at the side area (Figure 36b) shows similar effects, additionally a layer on the surface (4) can be seen. This layer was analyzed by an EDX-analysis in the SEM and the main parts are copper, nickel, tungsten, cobalt and magnesium. This mainly origin from the nickel sulfamate coating, which was done to increase the adhesion of the brazing, and the brazing material CuNi_3 . Other elements represent crushed tungsten carbides and binder residues, mixed with some minerals from the base material. The surface along the side in detail (Figure 36d) mainly consists of rounded carbide grains and some cracks in the grains, tending to have the direction parallel to the surface.

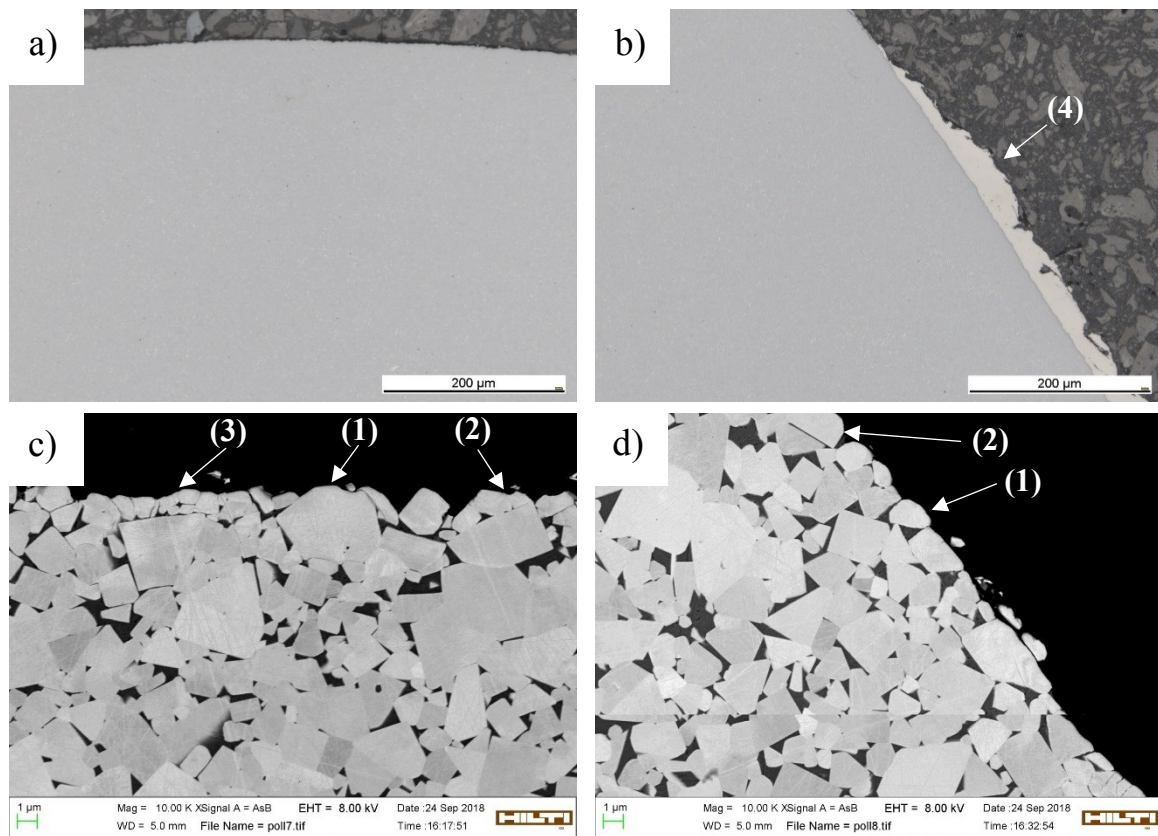


Figure 36: Microscopic analysis of grade B1-6Co after application testing. LOM images of the a) tip area and b) side area; SEM images of the c) tip area and d) side area.

The surface at the tip of the B2-6Co grade (Figure 37a) is a bit rougher than the one of the grade B1-6Co and additionally shows some cracks underneath the surface. At the SEM image (Figure 37c) the before mentioned rounded carbide grains (1) are dominant, but moreover several crushed carbide (3) grains can be detected. Similar mechanisms can be seen at the side area (Figure 37b and c). Furthermore, the LOM image of the side (Figure 37b) shows a different mechanism of wear, namely the release of a whole fragment (4) of carbide grains and cobalt binder. Moreover, a layer (5) consisting of residues of the nickel sulfamate coating, crushed cemented carbide and base material can be seen.

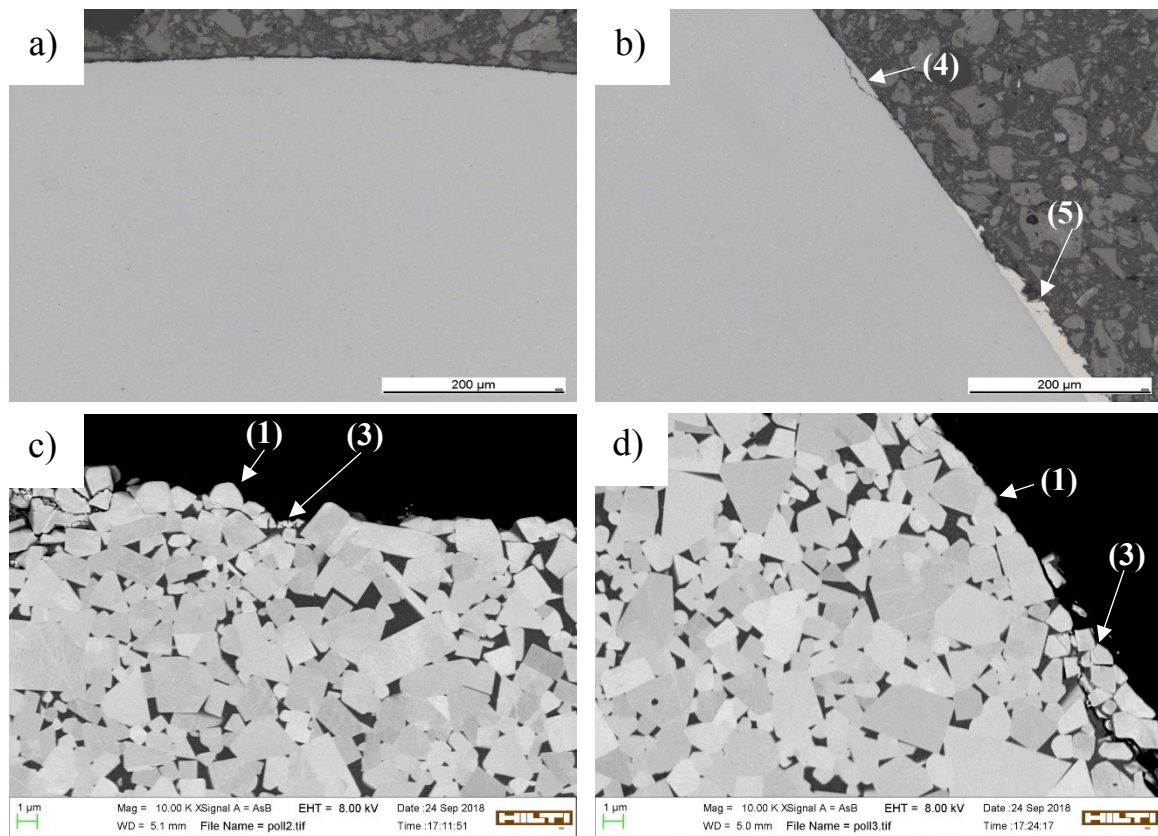


Figure 37: Microscopic analysis of grade B2-6Co after application testing. LOM images of the a) tip area and b) side area; SEM images of the c) tip area and d) side area.

In contrast to the described material grades before, the grade B3-6Co has a different geometry and pin shape. Figure 38a reveals a massive degradation by impact spalling on the tip surface of the tested pin. Numerous cracks underneath the surface and the detachment of composite scale fragments at the tip area can be detected. A closer look (Figure 38c) again shows rounded carbide grains (1), but the crushing of these grains (3) and the release of whole fragments is predominant. At the side area Figure 38b shows also degradation by impact spalling and cracks underneath the surface, but in a minor extent. The appearance of the side area in detail (Figure 38d) is similar to the tip area, but it clearly shows a flatter surface, moreover, the cracks in the carbide grains (2) are tending to be parallel to the surface plane.

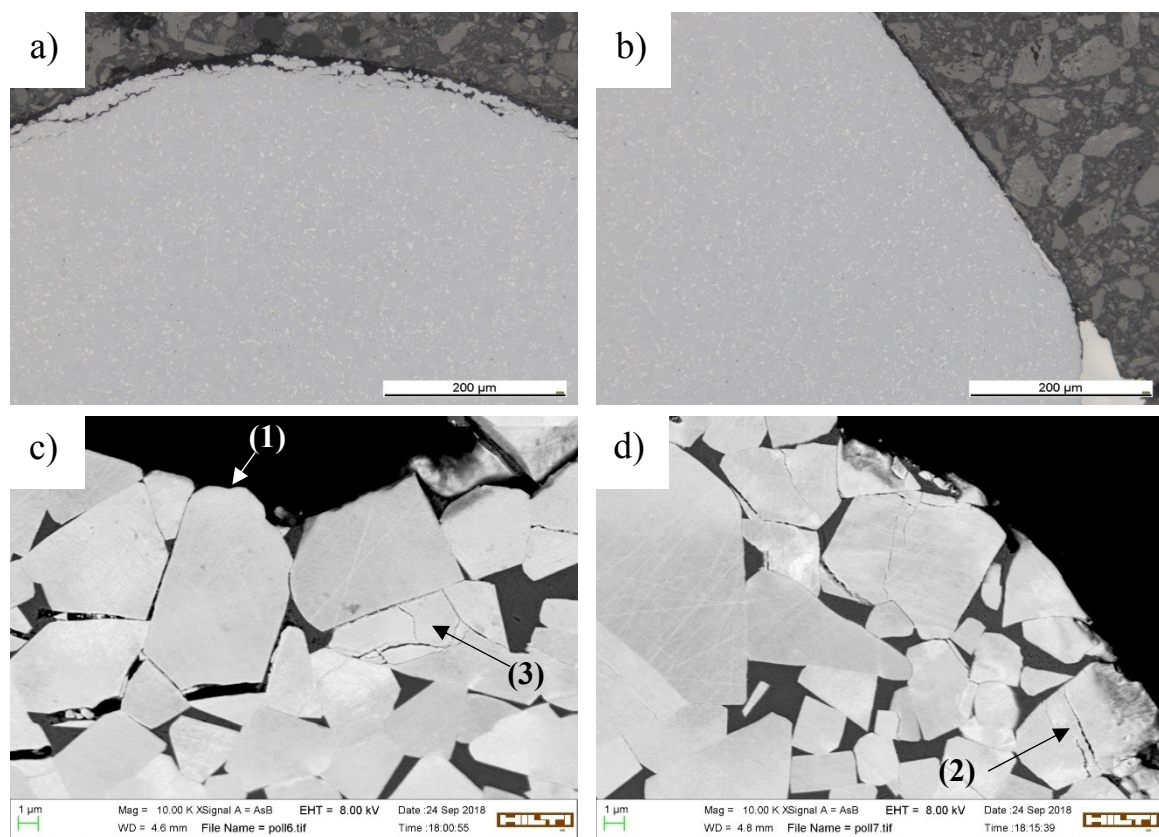


Figure 38: Microscopic analysis of grade B3-6Co after application testing. LOM images of the a) tip area and b) side area; SEM images of the c) tip area and d) side area.

For the grade B4-9.5Co the surface (Figure 39a) of the tested pins looks relatively smooth in the cross-section at the tip. A detachment of a whole fragment of cemented carbide (4) can be observed. Figure 39c shows rounded carbide grains (1) but also some cracks (2) in the grains along the surface. The surface of the side area ((Figure 39b) looks smooth, a closer look with the SEM ((Figure 39d) pictures numerous crushed carbide grains (3) at the side area. This could be initial surface carbide grains crushed by the impact during application, or adhered cemented carbide fragments originated from other locations of the pin.

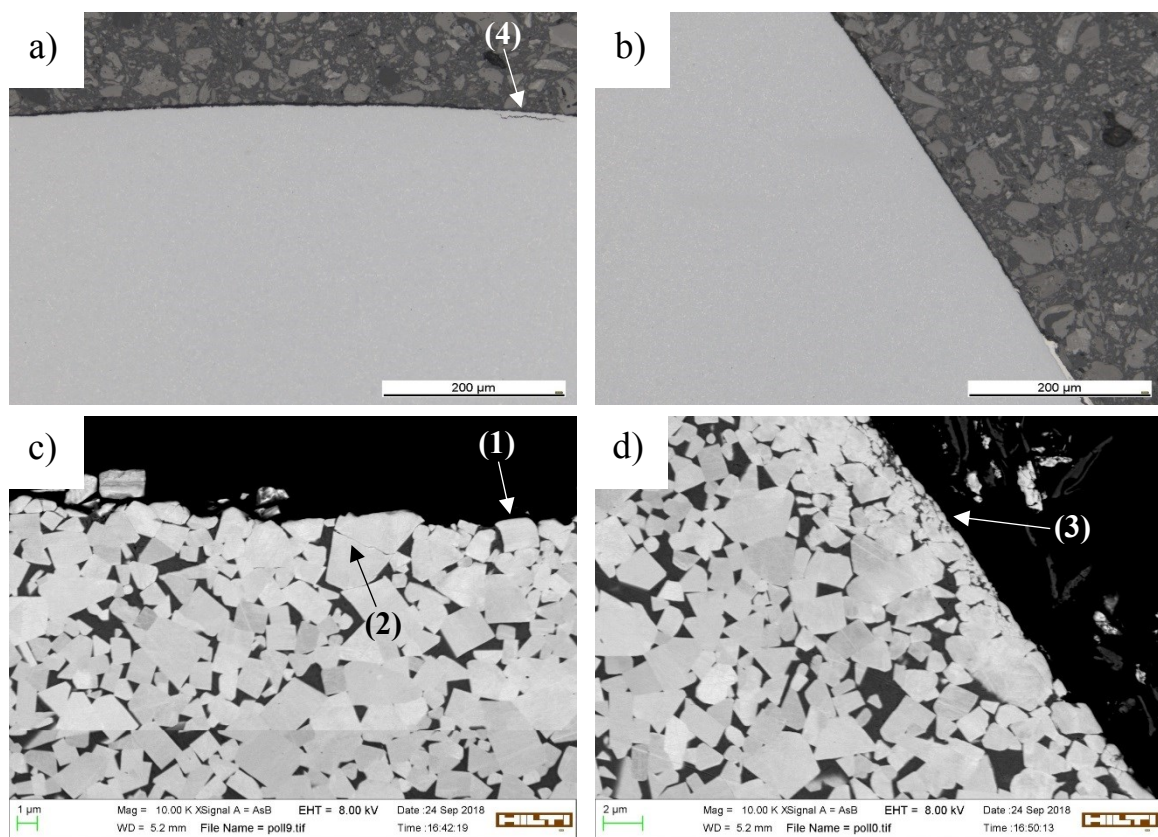


Figure 39: Microscopic analysis of grade B4-9.5Co after application testing. LOM images of the a) tip area and b) side area; SEM images of the c) tip area and d) side area.

At this point the microscopic analysis of the grade B5-9.5Co is described. Figure 40a shows impact spalling, breakout of single carbide grains and composite fragments, as well as several cracks under the surface. However, the degradation is not that massive like for the B3-6Co (Figure 38a). The SEM image of the tip area (Figure 40c) also reveals breakout of carbide grains and many cracked grains. At the side of the tested B5-9.5Co pin there are equal mechanisms occurring, but the spalling is not that dominating and the surface appears smoother (Figure 40b). Also, the cracks in the carbide grains (2) parallel to the surface plane can be observed here (Figure 40d).

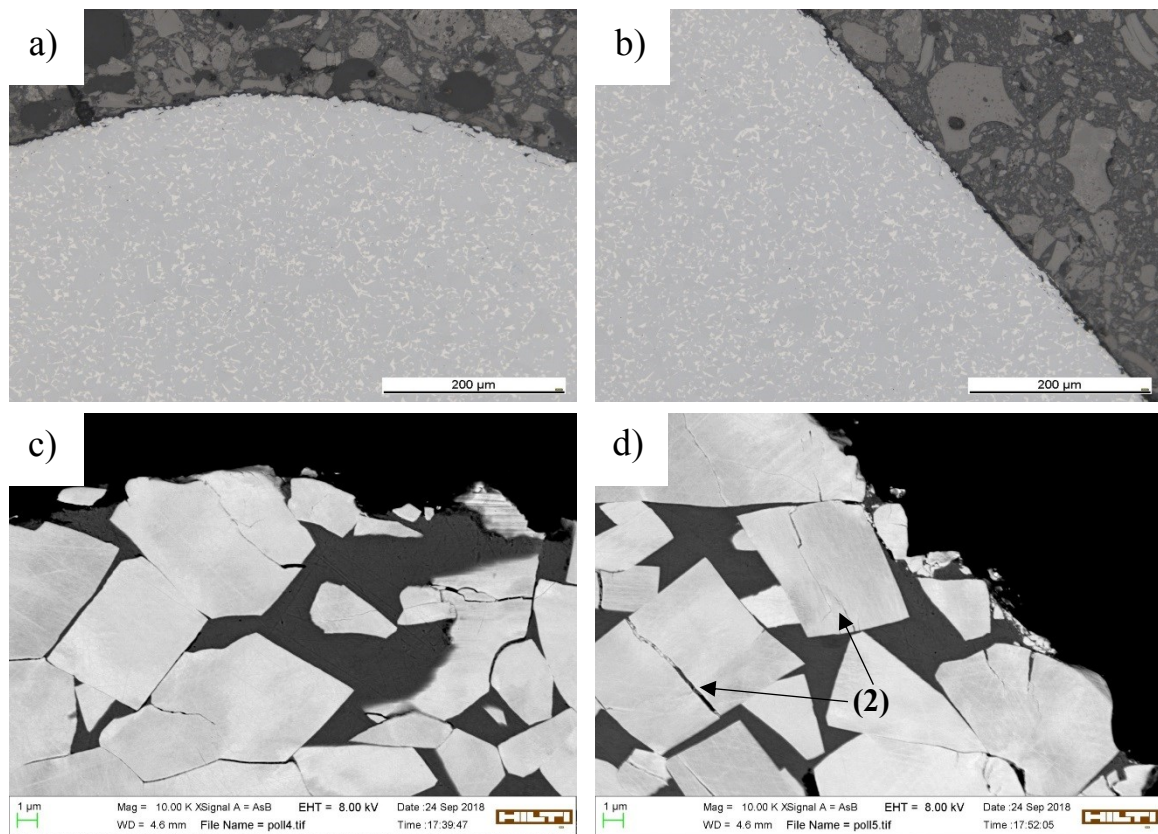


Figure 40: Microscopic analysis of grade B5-9.5Co after application testing. LOM images of the a) tip area and b) side area; SEM images of the c) tip area and d) side area.

5.4.1 Discussion of the results

Figure 33 illustrates the volume difference after 300 mm percussive demolition in the application testing. Basically, it clearly shows that the main volume loss is at the tip area of the cemented carbide pins. Comparing the grades B1-6Co and B2-6Co with similar geometries the latter reveals a higher volume loss, respectively wear rate. There was one breakage of a corner pin at the B2-6Co modified bushing tool, but this was taken in account for the following volume difference measurement. Regarding the grades B3-6Co and B5-9.5Co with similar geometries the grade with the higher binder content, namely B5-9.5Co, shows the higher volume loss. Finally, the unequal volume difference of the corner pin of the grade B4-9.5Co could be based on the inhomogeneous base material.

When it comes to the values of the volume difference, the percental volume loss was calculated to compensate the different pin sizes used for the application testing (see Table 7). The highest volume loss can be seen for the grade B5-9.5Co, followed at a distance from the grade B3-6Co. These are the grades with the coarsest tungsten carbide grain size and the sharpest shape. The correlation between the volume difference and the grain size is plotted in Figure 34, where a clear trend can be seen. The lowest volume loss is detected for the grade B1-6Co, in between the grade B2-6Co shows a little bit lower volume loss than the grade B3-6Co. These three grades have a quite similar grain size around 2 μm . At this point, it has to be taken into account that a breakout of a larger carbide grain leads to a higher volume loss than a breakout out if a smaller one.

To find a correlation between the wear rate of the B-grade cemented carbides during the application testing and the LCPC wear tests a plot is shown in Figure 35. The ranking of the different material grades regarding their volume difference, except for the quite similar grade B1-6Co and B2-6Co, is the same and a clear correlation is given.

Furthermore, the differences of the pin height also reveal the same ranking, as well as the increase of the tip angle (see Table 7). Due to its shape, there was no angle measured for the B4-9.5Co grade.

Regarding the microscopic analysis LOM and SEM images of the cross-section have been evaluated. Basically, the side area is smoother for all cemented carbide grades and pin geometries, most likely due to minor impact and more sliding contact in this area.

Comparing the different grades, those coming up with the smaller geometries (B1-6Co, B2-6Co) show a quite smooth appearance also at the tip area. Mainly rounded carbide grains and just a few cracks can be found. These grades also have the highest hardness values, and the highest number of pins on the head of the constructed modified bushing tool.

The grade B3-6Co shows the most deterioration with a massive degradation by impact spalling at the tip area. There are numerous cracks underneath the surface and break-outs of composite scale fragments can be observed. Slightly less degradation, but the same effects, reveals the grade B5-9.5Co, with a higher amount of cobalt binder. These two grades have the lowest hardness, but the sharpest geometry of all tested cemented carbide pins. Additionally, there are only five pins fixed on the modified bushing tool head due to their size.

The cross-section images of the B4-9.5Co pins show a relatively smooth overall surface with some cracks in the carbide grains. The hardness of this grade is between the values of the other grades. The round tip geometry could lead to a more gradual overall wear.

5.5 Analysis of the HILTI bushing tool

Additional to the cemented carbide pins of the B-grades analyzed after the application testing, worn pins of the HILTI bushing tool have been analyzed concerning their wear behavior and mechanisms.

The HILIT bushing tool is shown in Figure 3. The 25 pins of this tool consist out of a WC/Co grade with 9wt% binder content and a grain size between 0.8 – 2.5 μm , resulting in a hardness of about 1400HV10. The brazing material of the pin joining is CuSn6. The tools have been tested in a test rig on concrete C50/60 in horizontal direction, after a certain chiseling depth the tool was moved to the next position on the concrete. These tests have been executed externally, thus, the test parameters are not known in detail.

The following sections describe the results of the macroscopic and microscopic analysis on the cemented carbide pins of the HILTI bushing tool after application.

For the microscopic analysis, the light optical microscope was used to analyze the cross-section and Scanning Electron Microscope images have been done of the cross-sections and the surface. Due to the fine grain size, the light optical images do not give much relevant information. Thus, the focus was on the Scanning Electron Microscope. Figure 41 illustrates the analyzed pin areas, namely tip area and side area, for the microscopic analysis.

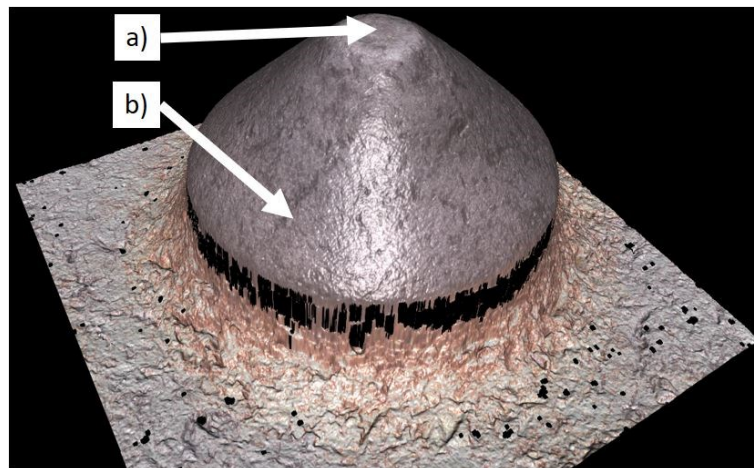


Figure 41: Areas of microscopic analysis: a) tip b) side

In the first step the HILTI bushing tools with different runtimes between ~3 and ~13 hours have been macroscopically analyzed. Representative results are shown in Figure 42 and Figure 43.

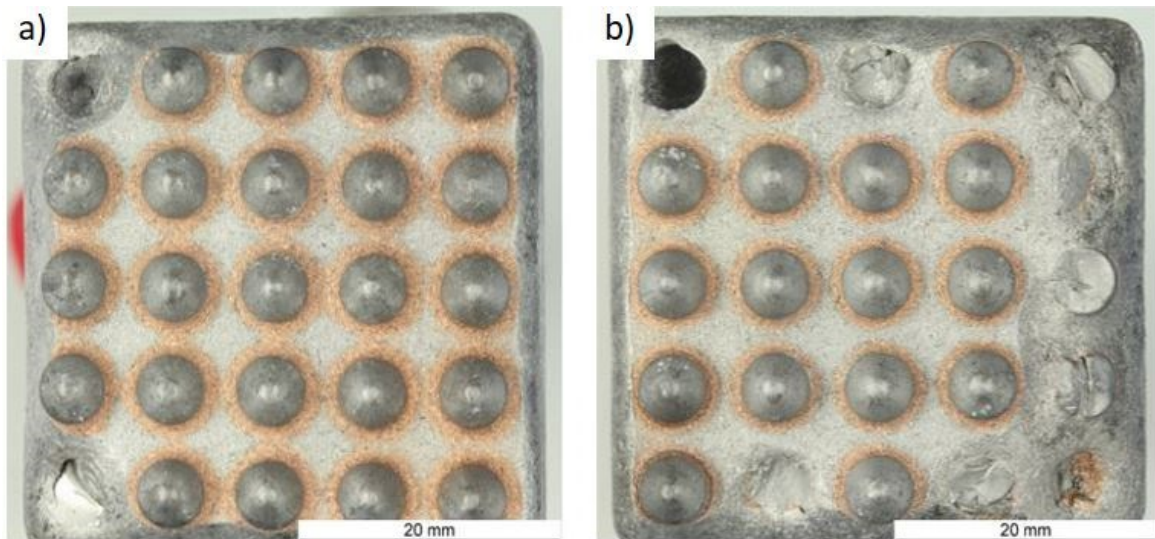


Figure 42: HILTI bushing tool tested in a test rig on concrete C50/60: a) ~3h b) ~13h

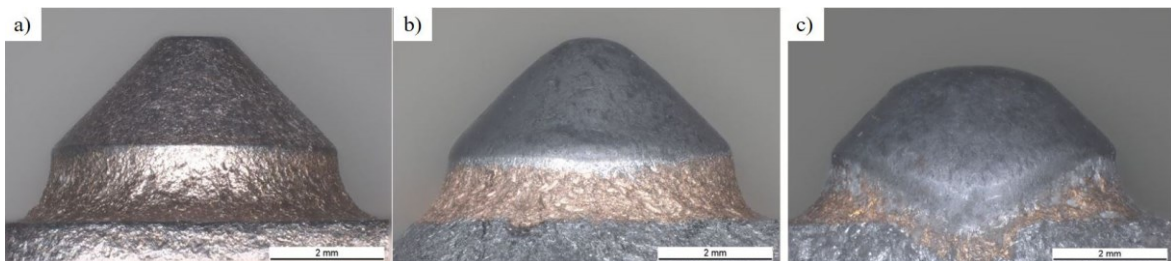


Figure 43: Cemented carbide pins of a HILTI bushing tool tested in a test rig on concrete C50/60: a) new b) runtime of ~3h c) runtime of ~13h

The macroscopic analysis shows up that with increasing runtime the risk of breakage or loss of a cemented carbide pin is also increasing (Figure 42), more frequently the breakage. The pins itself are getting smaller and rounder with increasing runtime (Figure 43).

The cross-section image of a new cemented carbide pin of a HILTI bushing tool is shown in Figure 44. Along the surface there is a thin layer ($\sim 6\mu\text{m}$) (1) consisting mainly of cobalt and the elements from the brazing material, namely copper and tin. From the surface, down to approximately $100\ \mu\text{m}$ a colored zone is visible, where a diffusion of the brazing material has taken place (2). Furthermore, in the bulk of the pins carbide agglomerations (3) can be seen. Especially the first mentioned layer may influence the wear behavior of these cemented carbide pins, due to that the diffusion zone possibly changing the mechanical properties of the material in this area.

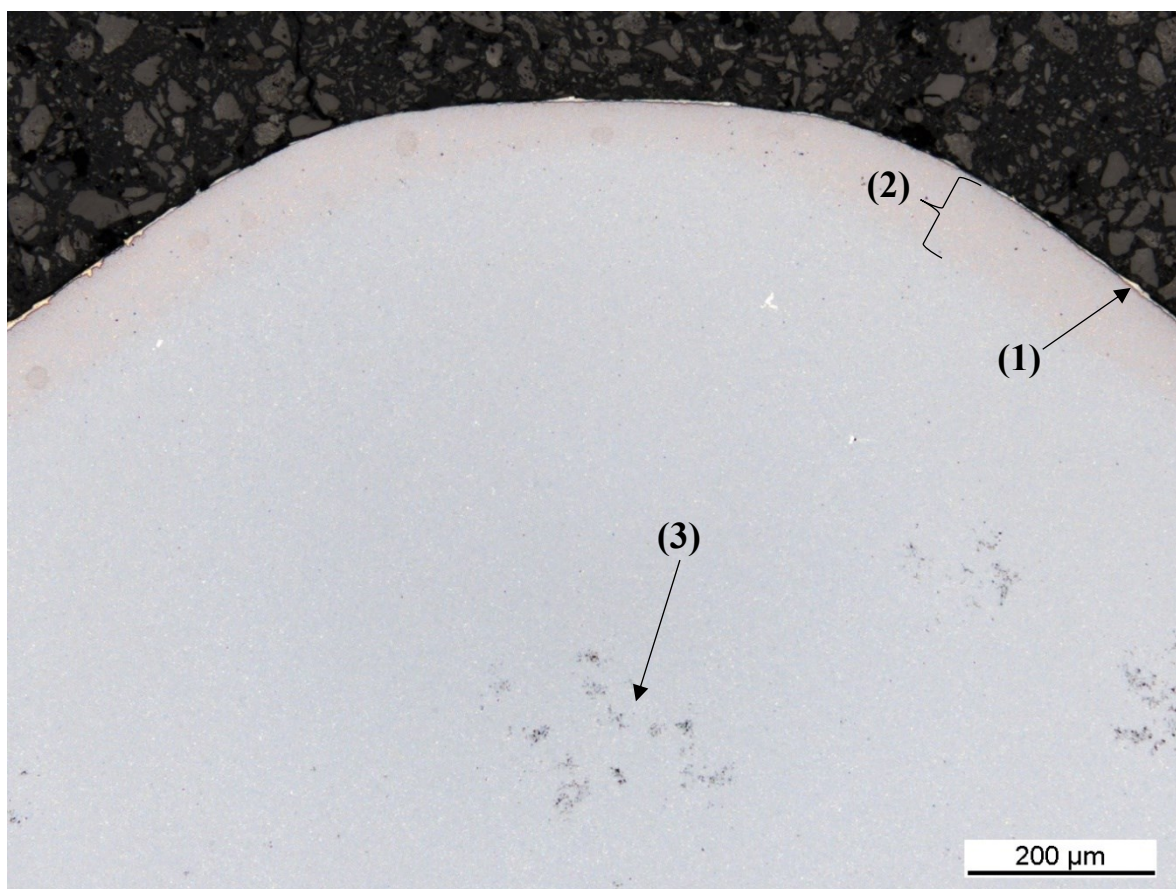


Figure 44: Cross-section of a new HILTI bushing tool

When looking at the surface images made by the Scanning Electron Microscope (Figure 45) the main phenomena are cracks in the carbide grains, crushed carbide grains and areas where a breakout of one or more carbide grains has taken place. There is neither a significant difference between the runtimes (3h vs 13h), nor between the different areas (tip vs side).

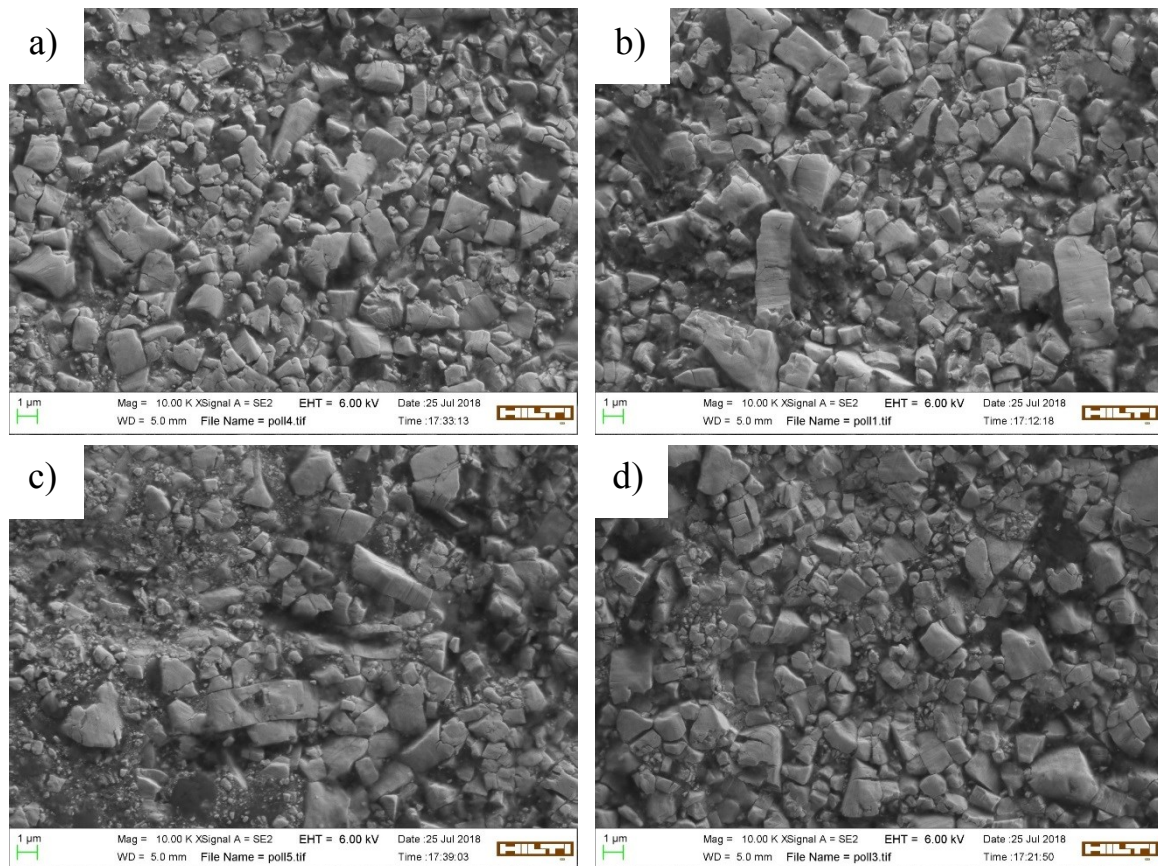


Figure 45: Surface images of worn cemented carbide pins of a HILTI bushing tool, showing the tip area after a runtime of a) ~3h, b) ~13h, and the side area after a runtime of c) ~3h, d) ~13h.

Coming to the cross-sections, there is also no apparent difference between the different runtimes of the tools. However, the carbide grains along the surface are rounded with just a few cracks, but there is a trend on the side area where the surface is smoother.

The EDX analysis (see Figure 46a) reveals that the area around S1 consists mainly of the binder material cobalt, but the grey colored area S2 contains mainly titanium, which is used as a grain growth inhibitor in cemented carbides.

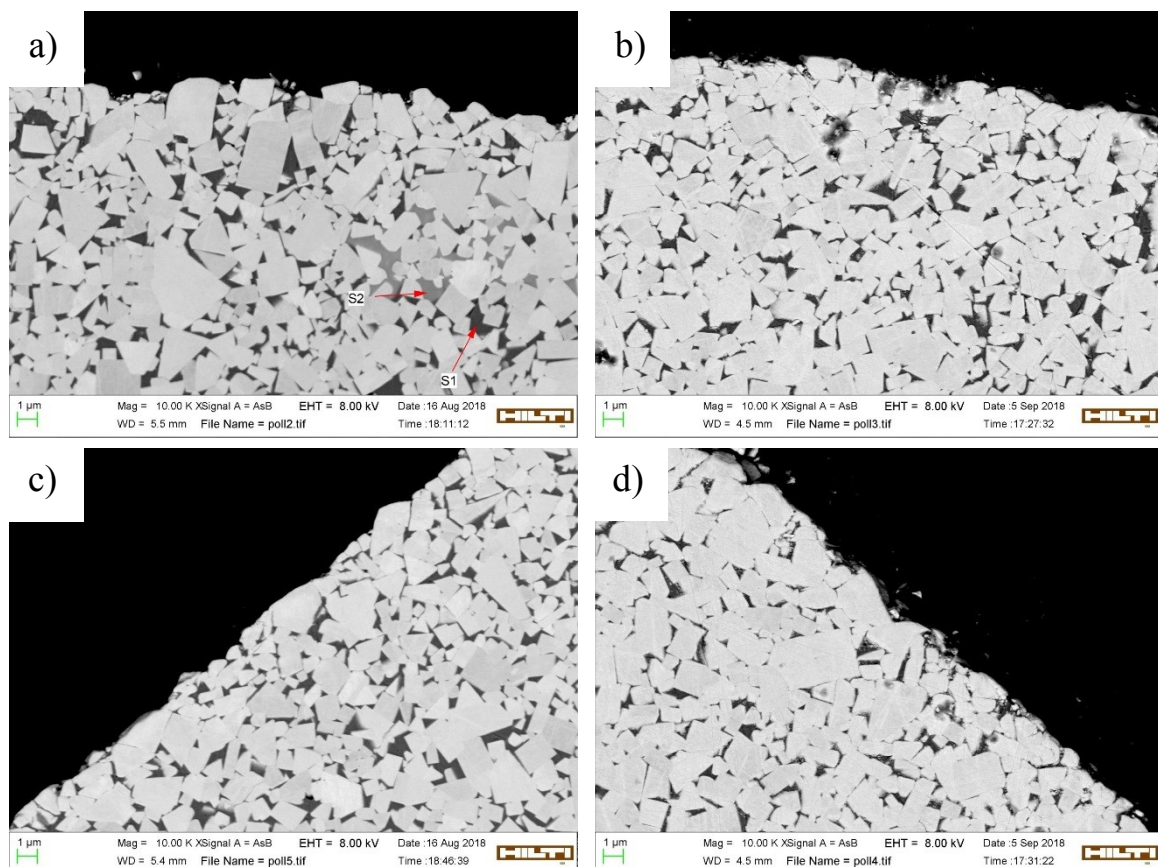


Figure 46: Cross-section images of worn cemented carbide pins of a HILTI bushing tool, showing the tip area after a runtime of a) ~3h, b) ~13h, and the side area after a runtime of c) ~3h, d) ~13h.

5.5.1 Discussion of the results

The macroscopic as well as the microscopic analysis reveals that there seems to be a gradual wear of the cemented carbide pins of the HILTI bushing tool. No significant differences can be detected between the runtimes (3h / 13h), merely a slightly smoother surface at the side. However, the unknown influence of the diffusion zone along the surface has to be taken into account in that case.

6 Summary, Conclusion and Future Work

6.1 Summary of the Results and Conclusions

In this work the wear behavior of ten different WC/Co cemented carbide grades, with differences in binder content and grain size, during percussive demolition was investigated.

In the first part, the average grain size and grain size distribution of every material grade was determined by the linear intercept procedure. The majority of the analyzed cemented carbide grades reveal an average grain size of approximately 2 μm , two grades have a coarser grain size of around 5 μm . Light optical microscope images with a magnification of 1000x show the microstructure of the different grades. Furthermore, the most important mechanical properties, namely the hardness and the fracture toughness were measured. For the latter, the Palmqvist method was used. Hardness values range from 987 HV30 up to 1425 HV30, Palmqvist fracture toughness values from 10.5 – 14.2 $\text{MPa}\sqrt{\text{m}}$. For the grades with the highest binder content and the ones with the coarsest grain sizes the Palmqvist fracture toughness was not possible to measure due to described limitations of this method.

Further edge toughness tests have been executed for every cemented carbide grade with the objective to find a correlation to parameters like grain size or binder content, and, to following laboratory or application tests. The calculated values for the edge toughness were around 3000 N/mm, but due to large deviations no significant correlation could be found with this test method. This is probably because the difficult sample preparation, especially when having quite small starting samples, but also due to quite similar tested materials.

The selected laboratory test method was the LCPC wear test. With this rotary wing test all ten different WC/Co grades have been tested in terms of their volume loss and wear rate. With the cuboid-shaped samples four tests with a duration of five minutes each have been executed. The results clearly correlate to the hardness of the material grade, more precisely the wear is increasing as hardness decreases, and the deviations are small. Hence, this test method offers a good opportunity to compare different cemented carbide grades in terms of their wear rate.

The next step was the application testing of different cemented carbide grades. For this, only the five B-grades had the necessary pin-shape to create a tool, which could be tested in a fully-automated 3-axis test rig. The tool used for this testing was a HILTI combi-hammer TE70.3 with an impact energy of 11.5 J and the base material was granite. The different material grades also came up with different shapes and sizes, hence, the chiseling depth was

adapted for each sample. Every cemented carbide grade was performing a percussive demolition of 300 mm in total.

Before the testing, optical 3D measurements have been performed, specifically, the height and the angle of the pins were measured. The illustrations of the volume difference measurement show the main volume loss at the tip of the pins. Regarding the percental volume difference, as well as the percental decrease of the pin height and increase of the tip angle, a clear ranking is evident. The grades with the coarser grain sizes reveal the highest wear rate, in addition they are the largest and sharpest pins. The volume loss of the smallest pins, equally the cemented carbide grades with higher hardness, was the lowest. It can be shown that there is a good correlation to the laboratory LCPC wear test. This also verify the possibility to test in the laboratory due to the same ranking in the application testing.

The microscopic analysis reveals that for the smaller pins, what means grades with hardness above 1400HV30 and fine grain size, the carbide grains at the tip surface get rounded and some cracks in the carbide grains are visible. The surface at the side of the pin appears smoother, but overall the difference between the tip and the side is not significant. The wear mechanisms are mainly grinding abrasion, and a few cracks in the carbide grains leading to minimal micro-spalling.

For the grades with the coarser grain sizes, which also have the sharpest and biggest geometries, there is a massive degradation at the top of the pins. The dominant wear mechanisms are impact spalling, detachment of whole WC grains and the detachment of composite scale fragments. The surface at the side appears smoother, showing crushing of WC grains and some detachment of fragments, but the main wear mechanism seems to be grinding abrasion. The cemented carbide grade with the round pin shape reveals not that obvious wear mechanisms. There are rounded WC grains, some cracks in the grains and crushing, even the detachment of composite scale fragments. However, the side shows again a smoother surface but with several crushed material.

Additionally, selected worn HILTI bushing tools, tested in an automated test rig on concrete, with runtimes between ~3 and ~13 hours have been analyzed concerning their wear behavior and mechanisms. The macroscopic analysis reveals that the cemented carbide pins of this tool are getting smaller and blunt with increasing runtime. The surface at the tip and the side was captured with the SEM, whereby the difference between selected runtimes and areas was not significant. Wear mechanism, like crushing of WC grains and breakout of single grains, can be identified. SEM images of the cross-section give more obvious information. The surface at the tip shows rounded carbide grains and a little crushing, while at the side the surface appears smoother and the wear mechanism grinding abrasion is dominating.

The results of the wear analysis of the HILTI bushing tool seem to be reasonably similar to the results of the similar shaped cemented carbide pins in the modified bushing tool application testing, which reveals a good correlation.

In this work, the wear mechanisms of WC/Co cemented carbides tested in automated test rig were identified. A good possibility to compare different cemented carbide grades concerning their wear with the laboratory LCPC wear test was proven, where the results not only show a clear correlation to hardness but also to the application testing. The analysis of the HILTI bushing tool verifies the results of the application testing, due to comparable wear mechanisms for similar geometries of the cemented carbide pins.

6.2 Future Work

To begin with, the significance of the edge toughness test could not be determined in this work, mainly due to the sample preparation. In future works the tests could be done with a narrow, machine sample preparation out of larger starting samples to ensure the exact geometry and angle. Hence, a correlation to the wear behavior in percussive demolition may be detected.

The LCPC wear test could be used in future works to compare alternative cemented carbide grades. There are also possibilities to test different shapes of the samples, which could be a possibility to rank them concerning their wear behavior.

Regarding the application testing there is a vast potential for future work, basically it was shown that the modified tool can show similar wear behavior as the HILTI bushing tool and the same ranking concerning wear rate as the LCPC wear test. Future work could be the testing of the same geometries but different cemented carbide grades, and, the testing of different geometries but the same material grade, to find correlations. Another work could be the testing of the same grade and geometry, but with different numbers of pins on the tool to point out possible differences. Finally, the application testing for the other five cemented carbide grades would be useful to show a correlation to the already available results from the laboratory LCPC wear test.

7 References

- [1] H. Exner, "Physical and chemical nature of cemented carbides," *International Metals Reviews*, pp. 149-173, 1979.
- [2] S. Nahak, S. Dewangan, S. Chattopadhyaya, G. Krolczyk and S. Hloch, "Discussion on importance of tungsten carbide - Cobalt (Wc-Co) cemented carbide and its critical characterization for wear mechanisms based on mining applications," *Archives of Mining Sciences*, vol. 63, no. 1, pp. 229-246, 2018.
- [3] U. Beste and S. Jacobson, "A new view of the deterioration and wear of WC/Co cemented carbide rock drill buttons," *Wear*, vol. 264, pp. 1129-1141, 2008.
- [4] U. Beste, S. Jacobson and S. Hogmark, "Rock penetration into cemented carbide drill buttons during rock drilling," *Wear*, vol. 264, pp. 1142-1151, 2008.
- [5] "Standard terminology relating to wear and erosion," *ASTM G40-01*, 2001.
- [6] J. Archard, "Wear theory and mechanisms," in *Wear control handbook*, New York, ASME, 1980, pp. 35-80.
- [7] J. Burwell, "Survey of possible wear mechanisms," *Wear*, vol. 1, pp. 119-140, 1958.
- [8] M. Varenberg, "Towards a unified classification of wear," *Friction*, vol. 1, no. 4, pp. 333-340, 2013.
- [9] J. Larsen-Basse, "Wear of hard-metals in rock drilling: a survey of the literature," *Powder Metallurgy*, vol. 16, no. 13, pp. 1-32, 1973.
- [10] G. Upadhyaya, *Cemented tungsten carbides - Production, properties, and testing*, New Jersey: Noyes publications, 1998.
- [11] H. Engqvist, "Microstructural aspects on wear of cemented carbides," Department of Materials Physics - Tribomaterials Group, Uppsala University, Uppsala, 2000.
- [12] U. Beste, T. Hartzell, H. Engqvist and N. Axén, "Surface damage on cemented carbide rock-drill buttons," *Wear*, vol. 249, pp. 324-329, 2001.
- [13] H. Engqvist and U. Wiklund, "Mapping of mechanical properties of WC-Co using nanoindentation," *Tribology Letters*, vol. 8, pp. 147-152, 2000.
- [14] S. Nahak, S. Dewangan and S. Chattopadhyaya, "Discussion on wear phenomena in cemented carbide," *Procedia Earth and Planetary Science*, vol. 11, pp. 284-293, 2015.
- [15] U. Beste, "On the nature of cemented carbide wear in rock drilling," *Comprehensive Summaries of Uppsala Dissertations from the Faculty of Science and Technology 964*, Uppsala, 2004.

-
- [16] D. O'Quigley, S. Luyckx and M. James, "An empirical ranking of a wide range of WC-Co grades in terms of their abrasion resistance measured by the ASTM standard B 611-85 test," *International Journal of Refractory Metals & Hard Materials*, vol. 15, pp. 73-79, 1997.
- [17] Z. Z. Fang, "Correlation of transverse rupture strength of WC-Co with hardness," *International journal of refractory metals & hard materials*, vol. 23, pp. 119-127, 2005.
- [18] "www.matweb.com," [Online]. Available: <http://www.matweb.com/search/datasheet.aspx?matguid=3d4056a86e79481cb6a80c89caae1d90&ckck=1>. [Accessed 21 August 2018].
- [19] R. Montgomery, "The mechanism of percussive wear of tungsten carbide composites," *Wear*, vol. 12, pp. 309-329, 1968.
- [20] R. Montgomery, "Percussive wear properties of cemented carbides," *Transactions of the society of mining sciences of AIME*, vol. 244, pp. 153-157, 1969.
- [21] R. Montgomery, A. Hara and T. Ikeda, "Influence of carbide grain size on percussive wear of cemented tungsten carbide rock bit inserts," *Transactions of the society of mining sciences of AIME*, vol. 244, pp. 136-138, 1970.
- [22] S. Bailey and C. Perrott, "Wear processes exhibited by WC-Co rotary cutters in mining," *Wear*, vol. 29, pp. 117-128, 1974.
- [23] R. Blombery, C. Perrott and P. Robinson, "Similarities in the mechanisms of wear of tungsten carbide-cobalt tools in rock and metal cutting," *Wear*, vol. 27, pp. 383-390, 1973.
- [24] J. Larsen-Basse, "Abrasion of WC-Co alloys by quartz," *Journal of lubrication technology*, vol. 101, pp. 208-211, 1979.
- [25] C. Perrott, "Tool materials for drilling and mining," *Annual review of materials science*, vol. 9, pp. 23-50, 1979.
- [26] U. Beste and S. Jacobson, "Targeting micro-sectioning - a technique to study subsurfaces features in worn specimens," *Wear*, vol. 264, pp. 1152-1156, 2008.
- [27] U. Beste, H. Engqvist and S. Jacobson, "Pressure cycling induced modification of a cemented carbide," *Proceedings of the 15th International Plansee Seminar, Reutte*, vol. 2, pp. 685-697, 2001.
- [28] J. Larsen-Basse, C. M. Perrott and P. M. Robinson, "Abrasive wear of tungsten carbide - cobalt composites. 1. Rotary drilling tests," *Materials Science and Engineering*, vol. 13, pp. 83-91, 1974.
- [29] B. Lomborg, *The skeptical environmentalist: Measuring the real state of the world*, Cambridge; UK: Cambridge University Press, 2001.

-
- [30] B. Mather, "Realizing the potential of concrete as a construction material," in *Proceedings of the International congress 'Creating with Concrete' at University of Dundee*, Dundee, UK, 1999.
- [31] "www.betontechnische-daten.de," HeidelbergCement AG, [Online]. Available: <https://www.betontechnische-daten.de/de/6-2-3-druckfestigkeitsklassen>. [Accessed 20 August 2018].
- [32] S. K. Haldar and J. Tisljar, *Introduction to mineralogy and petrology*, Waltham, USA: Elsevier, 2014.
- [33] H. Blatt and R. J. Tracy, "Petrology - Igneous, sedimentary, and metamorphic," *Geological Magazine*, vol. 134, pp. 121-142, 1997.
- [34] N. P. Laboratory, "Measurement good practice guide No.20 - Mechanical tests for hardmetals," London, UK.
- [35] National Physical Laboratory, "Measurement good practice guide No.9 - Palmqvist toughness for hard and brittle materials," London, UK, 1998.
- [36] E. A. Almond and N. J. McCormick, "Constant-geometry edge-flaking of brittle materials," *Nature*, vol. 321, pp. 53-55, 1986.
- [37] R. Danzer, M. Hangl and R. Paar, "Edge chipping of brittle materials - Fractography of Glasses and Ceramics IV," *Ceramic Transactions*, pp. 43-55, 2001.
- [38] N. F. P18-579, *Granulats: Essai d'abrasivité et de broyabilité*, Paris: AFNOR Association française de normalisation, 1990.
- [39] R. J. Plinninger and U. Restner, "Abrasivity testing, quo vadis? - A commented overview of abrasivity testing methods," *Geomechanik und Tunnelbau*, vol. 1, no. 1, pp. 61-70, 2008.
- [40] D. Tkalich, A. Kane, A. Saai, V. A. Yastrebov, M. Hokka, V. Kuokkala, M. Bengtsson, A. From, C. Oelgardt and C. C. Li, "Wear of cemented tungsten carbide percussive drill-bit inserts: Laboratory and field study," *Wear*, Vols. 386-387, pp. 106-117, 2017.
- [41] "www.hilti.com," HILTI AG, [Online]. Available: <https://www.hilti.com/drilling-&-demolition/combihammers/r1021424>. [Accessed 21 August 2018].
- [42] S. Moseley, S. Momeni, C. Peters, G. Domani and J. Allaart, "The influence of loading spectrum, workpiece material, hardmetal grade and drillbit design on the wear and fracture mechanisms of drill bits during rotary-percussive drilling of reinforced concrete: experimental studies and FEM," in *WorldPM2016*, Hamburg, Germany, 2016.
- [43] L. Reimer, *Scanning electron microscopy - Physics of image formation and microanalysis*, Berlin Heidelberg: Springer-Verlag, 1998.

- [44] T. Heinig, "www.hzdr.de," Helmholtz - Zentrum Dresden Rossendorf, [Online]. Available: <https://www.hzdr.de/db/Cms?pNid=67&pLang=de>. [Accessed 24 August 2018].
- [45] A. E112-12, Standard test methods for determining average grain size, West Conshohocken, USA: ASTM International, 2013.

LIST OF TABLES

Table 1: Average of the chemical composition of granite [33].....	14
Table 2: Selected specifications of investigated WC/Co cemented carbide grains.....	24
Table 3: Average grain size of investigated WC/Co cemented carbide determined by the lineal intercept procedure according to [45].....	28
Table 4: Results of the hardness measurements and Palmqvist fracture toughness determination.....	29
Table 5: Results of the edge toughness testing.....	32
Table 6: Dimension of the application tested cemented carbide grades.....	38
Table 7: The calculated percental differences of the height, angle and volume of the different cemented carbide grades during application testing (300 mm in granite).....	40

LIST OF FIGURES

Figure 1: Microstructure of WC-9.5 wt% Co cemented carbide.....	2
Figure 2: Drill bits for rotary percussion drilling [2].....	3
Figure 3: HILTI bushing tool with cemented carbide pins	3
Figure 4: Summary of pathological wear types determined by relative motion and surface disturbance by [8].	5
Figure 5: The hexagonal WC crystal structure [15].	7
Figure 6: Plots of the hardness of different WC-Co grades vs the cobalt content, at approximately constant grain size. The grain size of the tungsten carbides is classified in UF (ultra-fine), F (fine), M (medium) and C (coarse) [16].	7
Figure 7: Correlation between fracture toughness and hardness for WC/Co cemented carbides [17].	8
Figure 8: Correlations between TRS and a) hardness, and b) fracture toughness [17].	8
Figure 9: Schematic illustration of five important mechanisms of material removal of rock drill buttons. (a) Crushing of WC grains and release of fragments. (b) Detachment of whole or parts of WC grains (c) Crushing and removal of binder/rock mixture (d) Tribochemical wear of the carbides (e) Detachment of composite scale fragments [3].	13
Figure 10: a) Schematic diagram and definitions for the Palmqvist method. b) Comparison of Palmqvist toughness values with plane strain fracture toughness K_{Ic} [35].	15
Figure 11: Edge toughness testing machine [37].	17
Figure 12: Schematic drawing where distance from the edge of the loading point is pictured a) before, and b) after the test [37].	18
Figure 13: Testing aperture for the LCPC Abrasivity test [39].	19
Figure 14: Modified impeller for testing cemented carbide samples by the LCPC Abrasivity test.....	19
Figure 15: Fully automated 3-axis test bench situated at HILTI AG Headquarters in Schaan, FL. A combi-hammer tool is already installed, to start the test program a specific chisel and base material must be inserted in the next steps.	20
Figure 16: Wear intensity assessment reference pictures, the upper images represent a coarse grained cemented carbide, the lower a fine grained. a) fatigue/abrasion intensity "0", b) fatigue intensity "1", c) fatigue intensity "3", d) fatigue/abrasion intensity "0", e) abrasion intensity "1.5", f) abrasion intensity "3" [42].	21
Figure 17: a) Alicona TM measurement equipment, Visualization of a b) unworn and c) worn WC/Co cemented carbide pin of a HILTI bushing tool.	22
Figure 18: Interactions between the primary electron beam and the investigated sample surface [44].	23

Figure 19: Microstructure captured with a Leica DM6000M and a magnification of 100x of a) A1-6Co b) A2-8Co c) A3-8.5Co d) A4-10Co e) A5-11Co.....	25
Figure 20: Microstructure captured with a Leica DM6000M and a magnification of 100x of a) B1-6Co b) B2-6Co c) B3-6Co d) B4-9.5Co e) B5-9.5Co.....	26
Figure 21: Grain size distribution for the A-grades cemented carbides.....	27
Figure 22: Grain size distribution for the B-grades cemented carbides.....	27
Figure 23: Determined Palmqvist fracture toughness over measured hardness values.....	30
Figure 24: Edge toughness testing machine ET500	31
Figure 25: a) A valid result of an edge flake test on the left side of the sample, an invalid on the right. b) An example of the distance measurement of the loading point from the edge of the sample after a test.	31
Figure 26: Correlation between the edge toughness and the determined Palmqvist fracture toughness of the investigated cemented carbide grades.....	32
Figure 27: LCPC testing machine C.E.T.E de l'ouest, Abroy, Type 461B, No.: 39.	34
<i>Figure 28: A-grades results of the LCPC wear test.</i>	<i>35</i>
<i>Figure 29: B-grades results of the LCPC wear test.</i>	<i>35</i>
<i>Figure 30: Correlation between the volume loss during the LCPC wear tests and the measured hardness. The volume difference measurement was started at the second test to avoid influences of the starting steel plate.</i>	<i>36</i>
Figure 31: The different geometries of the pins for the application testing (from left to right): B2-6Co, B1-6Co, B4-9.5Co, B3-6Co and B5-9.5Co.	37
Figure 32: The modified bushing tool heads for the grade a) B1-6Co, b) B2-6Co, c) B3-6Co, d) B4-9.5Co and e) B5-9.5Co. f) shows the whole modified bushing tool for the grade B4-9.5Co.	38
Figure 33: The visualization of the volume difference measurements of the modified bushing tools during application testing (300 mm in granite) for the grade a) B1-6Co, b) B2-6Co, c) B3-6Co, d) B4-9.5Co and e) B5-9.5Co. It should be noted that the scale for the bigger pins (c)&e)) is different to the scale of the others.....	39
Figure 34 Correlation between the volume difference during the application testing and the grain size of the tested cemented carbide grades.....	40
Figure 35: Correlation between the volume difference during the application testing and the LCPC wear test.....	41
Figure 36: Microscopic analysis of grade B1-6Co after application testing. LOM images of the a) tip area and b) side area; SEM images of the c) tip area and d) side area.	42
Figure 37: Microscopic analysis of grade B2-6Co after application testing. LOM images of the a) tip area and b) side area; SEM images of the c) tip area and d) side area.	43
Figure 38: Microscopic analysis of grade B3-6Co after application testing. LOM images of the a) tip area and b) side area; SEM images of the c) tip area and d) side area.	44

Figure 39: Microscopic analysis of grade B4-9.5Co after application testing. LOM images of the a) tip area and b) side area; SEM images of the c) tip area and d) side area.....	45
Figure 40: Microscopic analysis of grade B5-9.5Co after application testing. LOM images of the a) tip area and b) side area; SEM images of the c) tip area and d) side area.....	46
Figure 41: Areas of microscopic analysis: a) tip b) side	49
Figure 42: HILTI bushing tool tested in a test rig on concrete C50/60: a) ~3h b) ~13h.....	50
Figure 43: Cemented carbide pins of a HILTI bushing tool tested in a test rig on concrete C50/60: a) new b) runtime of ~3h c) runtime of ~13h	50
Figure 44: Cross-section of a new HILTI bushing tool.....	51
Figure 45: Surface images of worn cemented carbide pins of a HILTI bushing tool, showing the tip area after a runtime of a) ~3h, b) ~13h, and the side area after a runtime of c) ~3h, d) ~13h.....	52
Figure 46: Cross-section images of worn cemented carbide pins of a HILTI bushing tool, showing the tip area after a runtime of a) ~3h, b) ~13h, and the side area after a runtime of c) ~3h, d) ~13h.	53
Figure 47: Grain size distribution determined by the lineal intercept procedure according to [45]. a) A1-6Co b) A2-8Co c) A3-8.5Co d) A4-10Co e) A5-11Co.....	73
Figure 48: Grain size distribution determined by the lineal intercept procedure according to [45]. a) B1-6Co b) B2-6Co c) B3-6Co d) B4-9.5Co e) B5-9.5Co	75

ANNEXES

A Test Reports

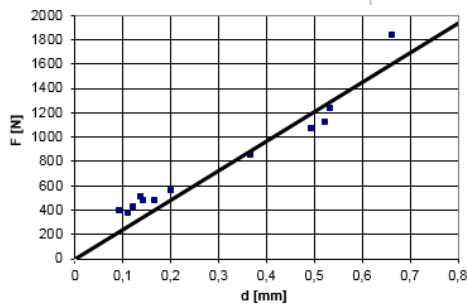
A1: Hardness and Palmqvist fracture toughness measurements

Grade	No.	I1 [μm]	I2 [μm]	I3 [μm]	I4 [μm]	Load [kg]	HV ₃₀	Warren und Matzke K _{IC}	HV ₃₀ Average		K _{IC} Average	
A1-6Co	1	61.0	63.0	69.0	80.0	30.0	1415	10.75	1389	± 17	10.82	± 0.2
	2	84.0	62.0	53.0	71.0	30.0	1378	10.66				
	3	64.0	63.0	58.0	84.0	30.0	1368	10.64				
	4	46.0	69.0	68.0	67.0	30.0	1400	11.17				
	5	75.0	58.0	55.0	71.0	30.0	1382	10.90				
A2-8Co	1	49.0	30.0	49.0	40.0	30.0	1296	13.11	1297	± 5	12.44	± 0.4
	2	57.0	40.0	40.0	59.0	30.0	1306	12.18				
	3	52.0	41.0	45.0	55.0	30.0	1296	12.23				
	4	46.0	45.0	46.0	42.0	30.0	1296	12.70				
	5	52.0	53.0	39.0	57.0	30.0	1292	11.97				
A3-8.5Co	1	60.0	53.0	60.0	69.0	30.0	1415	11.41	1413	± 4	11.64	± 0.2
	2	59.0	48.0	58.0	63.0	30.0	1412	11.75				
	3	70.0	48.0	53.0	66.0	30.0	1419	11.55				
	4	65.0	49.0	55.0	63.0	30.0	1408	11.63				
	5	64.0	50.0	51.0	56.0	30.0	1412	11.93				
A4-10Co	1					30.0	1165		1164	± 6		
	2					30.0	1160					
	3					30.0	1174					
	4					30.0	1157					
	5					30.0	1162					
A5-11Co	1					30.0	1185		1205	± 22		
	2					30.0	1197					
	3					30.0	1185					
	4					30.0	1242					
	5					30.0	1217					
B1-6Co	1	76.0	73.0	76.0	64.0	30.0	1412	10.43	1409	± 3	10.50	± 0.2
	2	65.0	73.0	73.0	71.0	30.0	1408	10.55				
	3	71.0	72.0	68.0	64.0	30.0	1411	10.69				
	4	74.0	82.0	72.0	73.0	30.0	1404	10.19				
	5	71.0	78.0	63.0	67.0	30.0	1412	10.62				
B2-6Co	1	51.0	61.0	66.0	68.0	30.0	1431	11.38	1425	± 10	11.74	± 0.4
	2	44.0	76.0	63.0	73.0	30.0	1434	11.17				
	3	55.0	75.0	57.0	41.0	30.0	1412	11.75				
	5	55.0	40.0	52.0	72.0	30.0	1435	12.08				
	6	53.0	72.0	59.0	47.0	30.0	1423	11.71				
	7	69.0	60.0	30.0	48.0	30.0	1412	12.33				

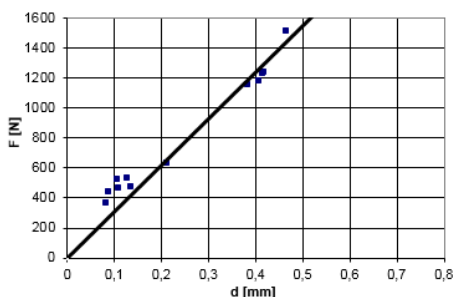
Grade	No.	I1 [μm]	I2 [μm]	I3 [μm]	I4 [μm]	Load [kg]	HV ₃₀	Warren und Matzke K _{IC}	HV ₃₀ Average		K _{IC} Average	
B3-6Co	1					30.0	1138		1150	± 15		
	2					30.0	1137					
	3					30.0	1154					
	4					30.0	1182					
	5					30.0	1139					
	6					30.0	1140					
	7					30.0	1171					
	8					30.0	1138					
	9					30.0	1148					
	10					30.0	1154					
B4-9.5Co	1	28.0	30.0	31.0	49.0	30.0	1292	14.44	1282	± 14	14.23	± 0.62
	2	28.0	31.0	30.0	41.0	30.0	1289	14.86				
	3	34.0	49.0	36.0	41.0	30.0	1267	13.28				
	4	18.0	28.0	40.0	42.0	30.0	1264	14.83				
	5	30.0	33.0	42.0	48.0	30.0	1299	13.75				
B5-9.5Co	1					30.0	978		987	± 14		
	2					30.0	969					
	3					30.0	1007					
	4					30.0	998					
	5					30.0	971					
	6					50.0	970					
	7					50.0	1003					
	8					50.0	990					
	9					50.0	983					
	10					50.0	1003					

A2: Edge toughness tests

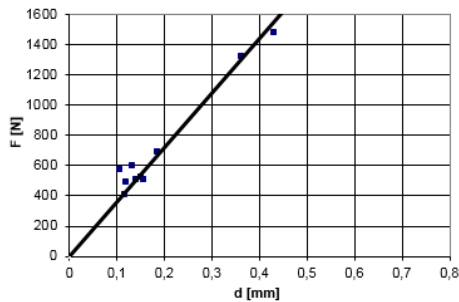
Edge chip resistance			Abstand	Kraft	F/d		
			d [mm]	[N]	[N/mm]		
Prüfung in radialer Richtung			Nr.	0	0		
Material:	A1-6Co		1	0,113	370	3274,34	
			2	0,122	426	3491,80	
			3	0,143	478	3342,66	
Datum:	05.07.2018		4	0,094	394	4191,49	
Belastungsgeschwindigkeit:	0,5 mm/min		5	0,523	1117	2135,76	
			6	0,498	1066	2140,56	
			7	0,534	1230	2303,37	
			8	0,139	506	3640,29	
Edge chip resistance [N/mm]: 2865 ± 672 (in Anlehnung an prTS 843-9)				9	0,168	470	2797,62
				10	0,203	557	2743,84
Edge chip resistance [N/mm]*):				11	0,664	1834	2762,05
*) durch lineare Regression ermittelt				12	0,495	1061	2143,43
				13	0,369	842	2281,84
				Mittelwert:	2865,31		
				Stabw:	672		



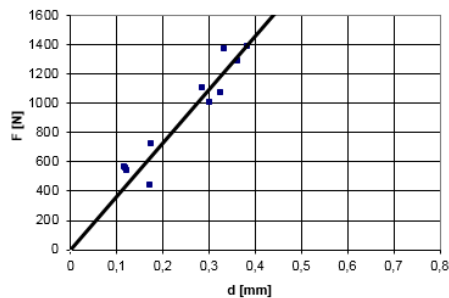
Edge chip resistance			Abstand	Kraft	F/d		
			d [mm]	[N]	[N/mm]		
Prüfung in radialer Richtung			Nr.	0	0		
Material:	A2-8Co		1	0,467	1510	3233,40	
			2	0,408	1174	2877,45	
			3	0,416	1228	2951,92	
Datum:	05.07.2018		4		1113		
Belastungsgeschwindigkeit:	0,5 mm/min		5	0,083	364	4385,54	
			6	0,089	440	4943,82	
			7	0,128	530	4140,63	
			8	0,108	516	4777,78	
Edge chip resistance [N/mm]: 3655 ± 786 (in Anlehnung an prTS 843-9)				9	0,419	1233	2942,72
				10	0,384	1147	2986,98
Edge chip resistance [N/mm]*):				11	0,136	468	3441,18
*) durch lineare Regression ermittelt				12	0,214	630	2943,93
				13	0,109	461	4229,36
				Mittelwert:	3654,56		
				Stabw:	786		



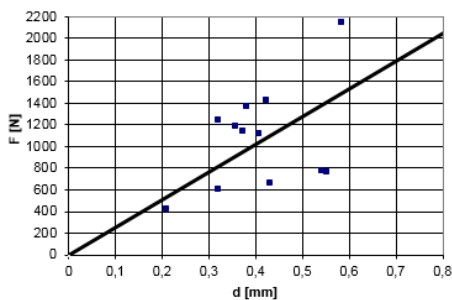
Edge chip resistance			Abstand	Kraft	F/d
			d [mm]	[N]	[N/mm]
Prüfung in radialer Richtung		Nr.	0	0	
		1		370	
Material:	A3-8.5Co	2	0,106	573	5405,66
		3		320	
Datum:	05.07.2018	4	0,133	594	4466,17
Belastungsgeschwindigkeit:	0,5 mm/min	5	0,186	683	3672,04
		6	0,141	501	3553,19
		7	0,432	1473	3409,72
Edge chip resistance [N/mm]: 3799 ± 636 (in Anlehnung an prTS 843-9)		8	0,362	1317	3638,12
		9	0,452	1632	3610,62
		10	0,157	502	3197,45
Edge chip resistance [N/mm]*):	3597	11	0,119	404	3394,96
*) durch lineare Regression ermittelt		12	0,121	487	4024,79
		13	0,152	519	3414,47
				Mittelwert:	3798,84
				Stabw:	636



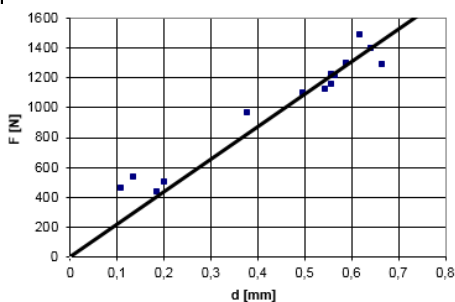
Edge chip resistance			Abstand	Kraft	F/d
			d [mm]	[N]	[N/mm]
Prüfung in radialer Richtung		Nr.	0	0	
		1	0,123	533	4333,33
Material:	A4-10Co	2	0,118	559	4737,29
		3	0,176	717	4073,86
Datum:	04.07.2018	4	0,121	554	4578,51
Belastungsgeschwindigkeit:	0,5 mm/min	5	0,384	1386	3609,38
		6	0,302	1001	3314,57
		7	0,363	1283	3534,44
Edge chip resistance [N/mm]: 3812 ± 642 (in Anlehnung an prTS 843-9)		8		455	
		9	0,334	1367	4092,81
		10	0,286	1098	3839,16
Edge chip resistance [N/mm]*):	3640,8	11	0,326	1068	3276,07
*) durch lineare Regression ermittelt		12	0,172	438	2546,51
		13			
				Mittelwert:	3812,36
				Stabw:	642



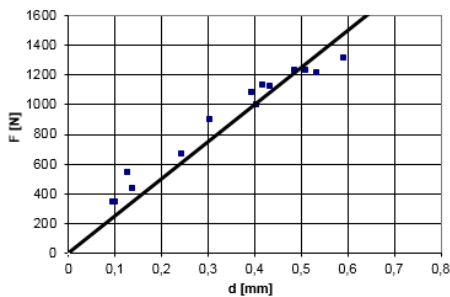
Edge chip resistance			Abstand	Kraft	F/d
			d [mm]	[N]	[N/mm]
Prüfung in radialer Richtung		Nr.	0	0	
Material:	A5-11Co	1	0,211	415	1966,82
		2	0,321	600	1869,16
		3	0,432	661	1530,09
Datum:	04.07.2018	4	0,543	768	1414,36
Belastungsgeschwindigkeit:	0,5 mm/min	5	0,553	760	1374,32
		6	0,585	2140	3658,12
		7	0,425	1420	3341,18
Edge chip resistance [N/mm]: 3812 ± 642 (in Anlehnung an prTS 843-9)		8	0,375	1133	3021,33
		9	0,408	1113	2727,94
		10	0,322	1237	3841,61
Edge chip resistance [N/mm]*):	2557,2	11	0,381	1360	3569,55
*) durch lineare Regression ermittelt		12	0,358	1182	3301,68
				Mittelwert:	2634,68
				Stabw:	944



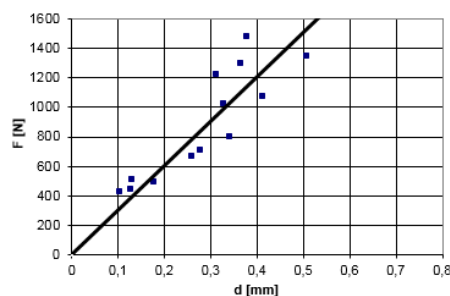
Edge chip resistance			Abstand	Kraft	F/d
			d [mm]	[N]	[N/mm]
Prüfung in radialer Richtung		Nr.	0	0	
Material:	B1-6Co	1	0,620	1488	2400,00
		2	0,109	460	4220,18
		3	0,136	530	3897,06
Datum:	03.07.2018	4	0,566	1215	2146,64
Belastungsgeschwindigkeit:	0,5 mm/min	5	0,203	495	2438,42
		6	0,667	1284	1925,04
		7	0,380	964	2536,84
Edge chip resistance [N/mm]: 2482 ± 690 (in Anlehnung an prTS 843-9)		8	0,546	1117	2045,79
		9		---	
		10	0,558	1221	2188,17
Edge chip resistance [N/mm]*):	2184	11	0,590	1294	2193,22
*) durch lineare Regression ermittelt		12		421	
		13	0,644	1393	2163,04
		14	0,559	1154	2064,40
		15	0,498	1097	2202,81
		16	0,186	432	2322,58
				Mittelwert:	2481,73
				Stabw:	690



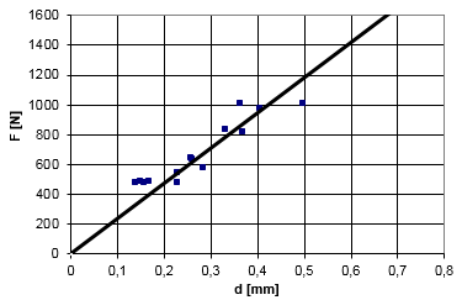
Edge chip resistance			Abstand	Kraft	F/d
			d [mm]	[N]	[N/mm]
Prüfung in radialer Richtung		Nr.	0	0	
Material:	B2-6Co	1	0,138	430	3115,94
		2	0,535	1214	2269,16
		3	0,096	341	3552,08
Datum:	04.07.2018	4	0,304	896	2947,37
Belastungsgeschwindigkeit:	0,5 mm/min	5	0,405	993	2451,85
		6	0,245	666	2718,37
		7		341	
Edge chip resistance [N/mm]: 2838 ± 554 (in Anlehnung an prTS 843-9)		8	0,512	1232	2406,25
		9	0,129	542	4201,55
Edge chip resistance [N/mm]*):	2500	10	0,593	1312	2212,48
*) durch lineare Regression ermittelt		11	0,435	1121	2577,01
		12	0,102	342	3352,94
		13	0,488	1228	2516,39
		14	0,419	1128	2692,12
		15	0,396	1077	2719,70
		Mittelwert:			2838,09
		Stabw:			554



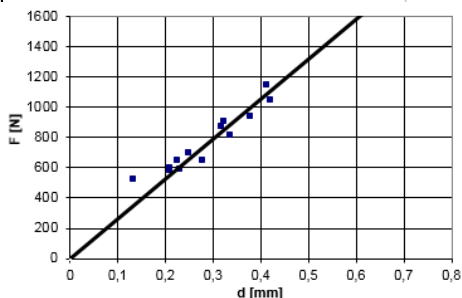
Edge chip resistance			Abstand	Kraft	F/d
			d [mm]	[N]	[N/mm]
Prüfung in radialer Richtung		Nr.	0	0	
Material:	B3-6Co	1	0,312	1219	3907,05
		2	0,328	1021	3112,80
		3	0,365	1295	3547,95
Datum:	03.07.2018	4	0,379	1475	3891,82
Belastungsgeschwindigkeit:	0,5 mm/min	5	0,131	503	3839,69
		6	0,178	493	2769,66
		7	0,279	707	2534,05
Edge chip resistance [N/mm]: 3172 ± 634 (in Anlehnung an prTS 843-9)		8	0,259	661	2552,12
		9	0,128	443	3460,94
Edge chip resistance [N/mm]*):	3016,7	10	0,341	793	2325,51
*) durch lineare Regression ermittelt		11		1466	
		12	0,508	1341	2639,76
		13	0,413	1071	2593,22
		14	0,105	427	4066,67
		Mittelwert:			3172,40
		Stabw:			634

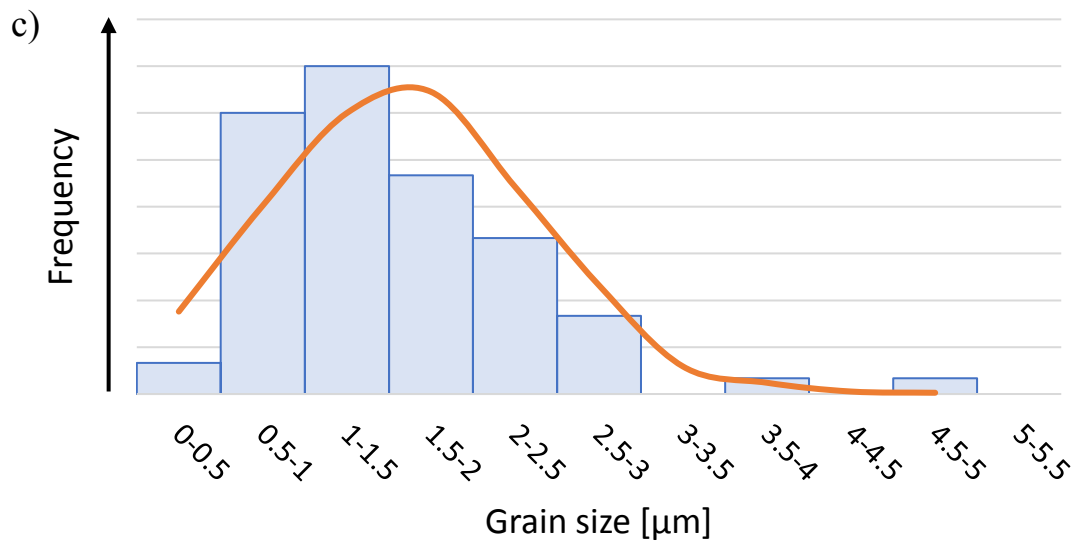
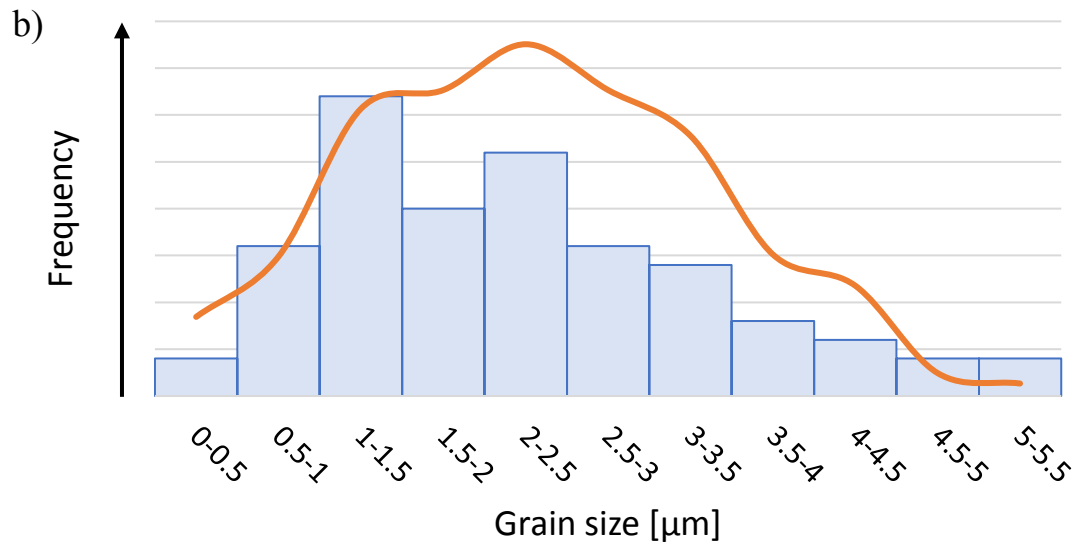
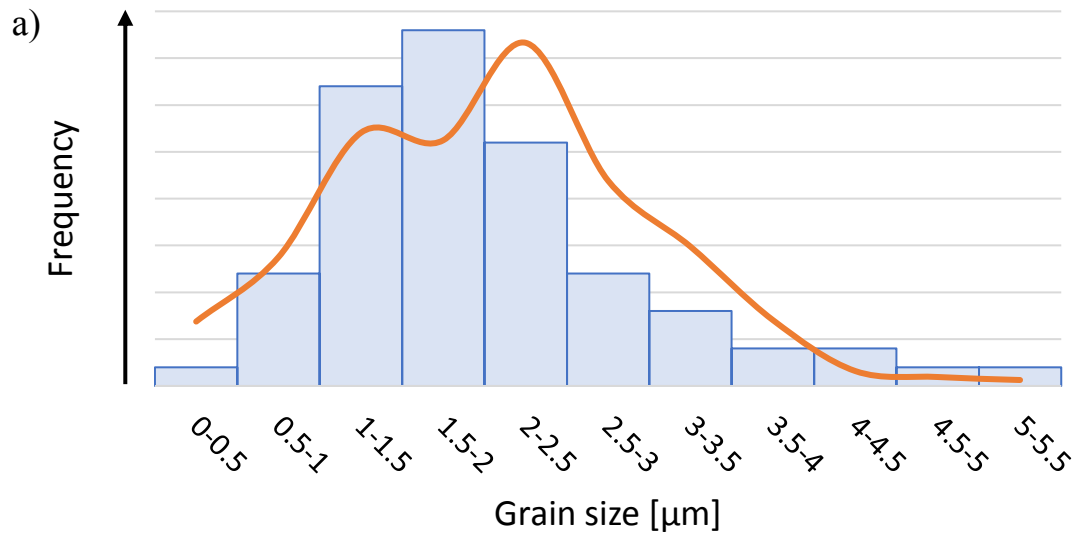


Edge chip resistance			Abstand d [mm]	Kraft [N]	F/d [N/mm]
Prüfung in radialer Richtung		Nr.	0	0	
Material:	<i>B4-9.5Co</i>	1	0,331	833	2516,62
		2	0,229	545	2379,91
		3		429	
Datum:	02.07.2018	4	0,159	471	2962,26
Belastungsgeschwindigkeit:	0,5 mm/min	5	0,151	479	3172,19
		6	0,139	478	3438,85
		7		1281	
Edge chip resistance [N/mm]: 2548 ± 437 (in Anlehnung an prTS 843-9)		8	0,284	575	2024,65
		9	0,262	630	2404,58
Edge chip resistance [N/mm]*):	2365	10	0,497	1004	2020,12
*) durch lineare Regression ermittelt		11	0,407	970	2383,29
		12	0,370	811	2191,89
		13	0,229	473	2065,50
		14	0,169	482	2852,07
		15	0,364	1004	2758,24
		16	0,258	644	2496,12
		Mittelwert:			2547,59
		Stabw:			437



Edge chip resistance			Abstand d [mm]	Kraft [N]	F/d [N/mm]
Prüfung in radialer Richtung		Nr.	0	0	
Material:	<i>B5-9.5Co</i>	1	0,380	933	2455,26
		2	0,337	814	2415,43
		3	0,226	644	2849,56
Datum:	02.07.2018	4	0,278	646	2323,74
Belastungsgeschwindigkeit:	0,5 mm/min	5		1315	
		6		1155	
		7	0,324	903	2787,04
Edge chip resistance [N/mm]: 2744 ± 388 (in Anlehnung an prTS 843-9)		8		1082	
		9	0,249	696	2795,18
		10		2120	
Edge chip resistance [N/mm]*):	2634,6	11		2482	
*) durch lineare Regression ermittelt		12		942	
		13	0,209	596	2851,67
		14	0,230	590	2565,22
		15	0,209	577	2760,77
		16			
		17	0,318	872	2742,14
		18	0,413	1141	2762,71
		19	0,134	521	3888,06
		20	0,421	1041	2472,68
		Mittelwert:			2743,80
		Stabw:			388



B Grain Size Distribution Figures

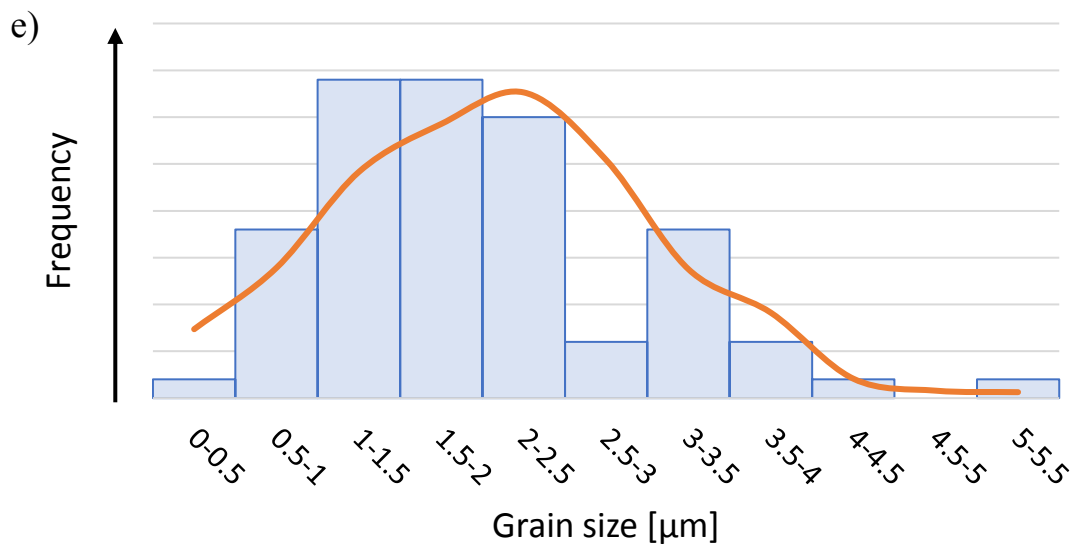
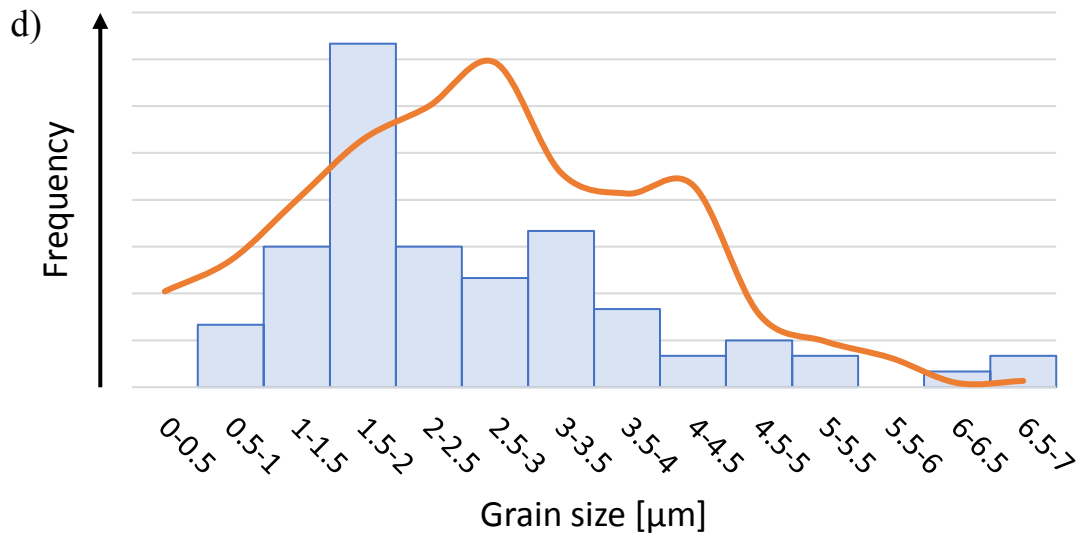
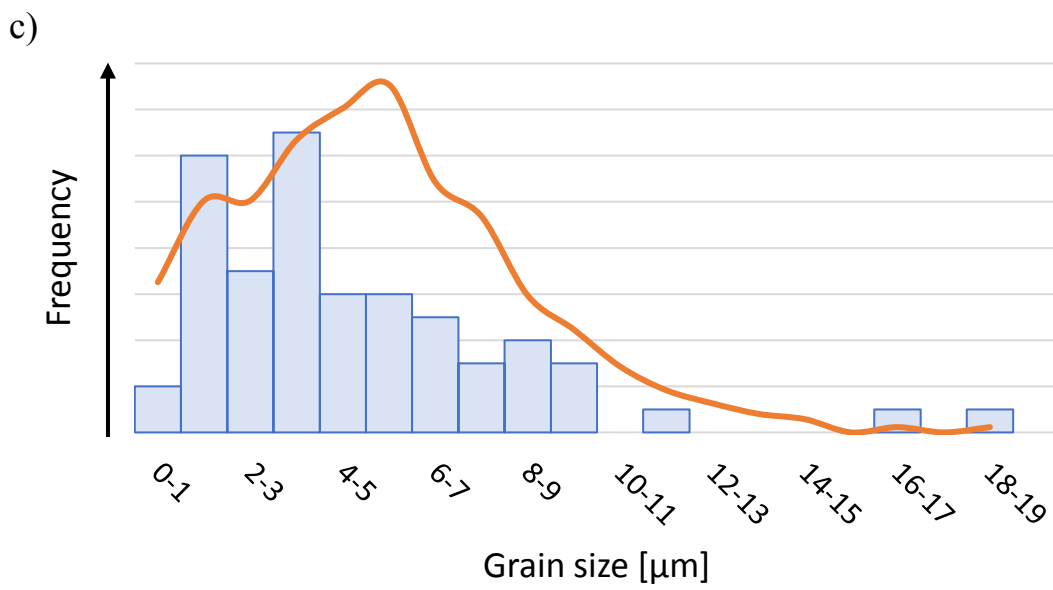
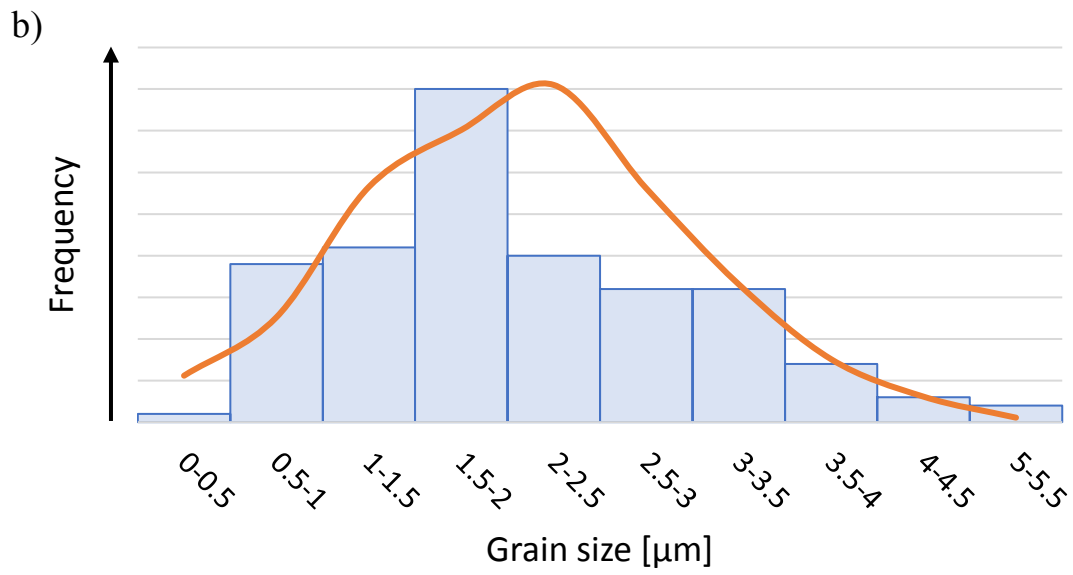
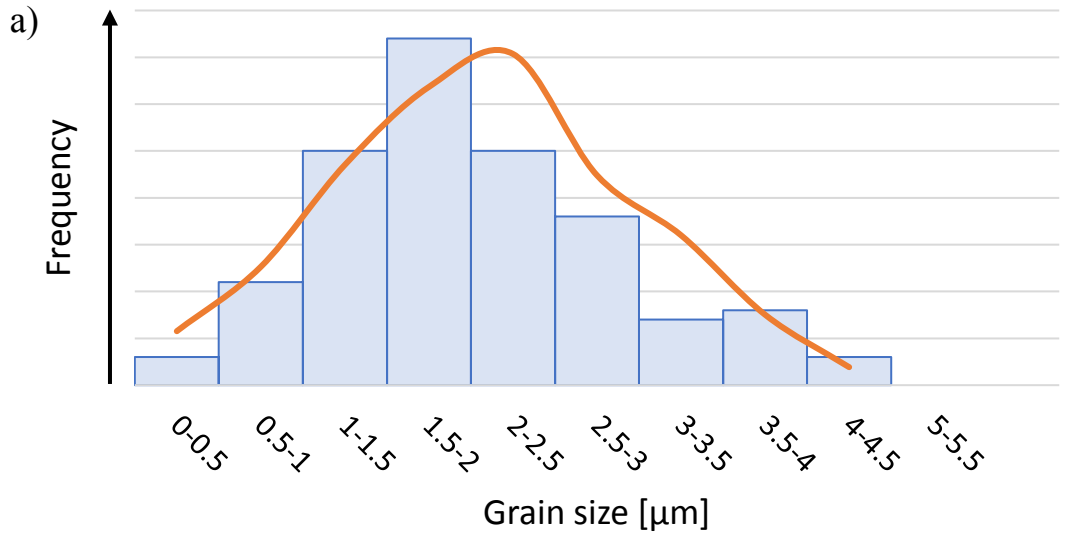


Figure 47: Grain size distribution determined by the lineal intercept procedure according to [45]. a) A1-6Co b) A2-8Co c) A3-8.5Co d) A4-10Co e) A5-11Co



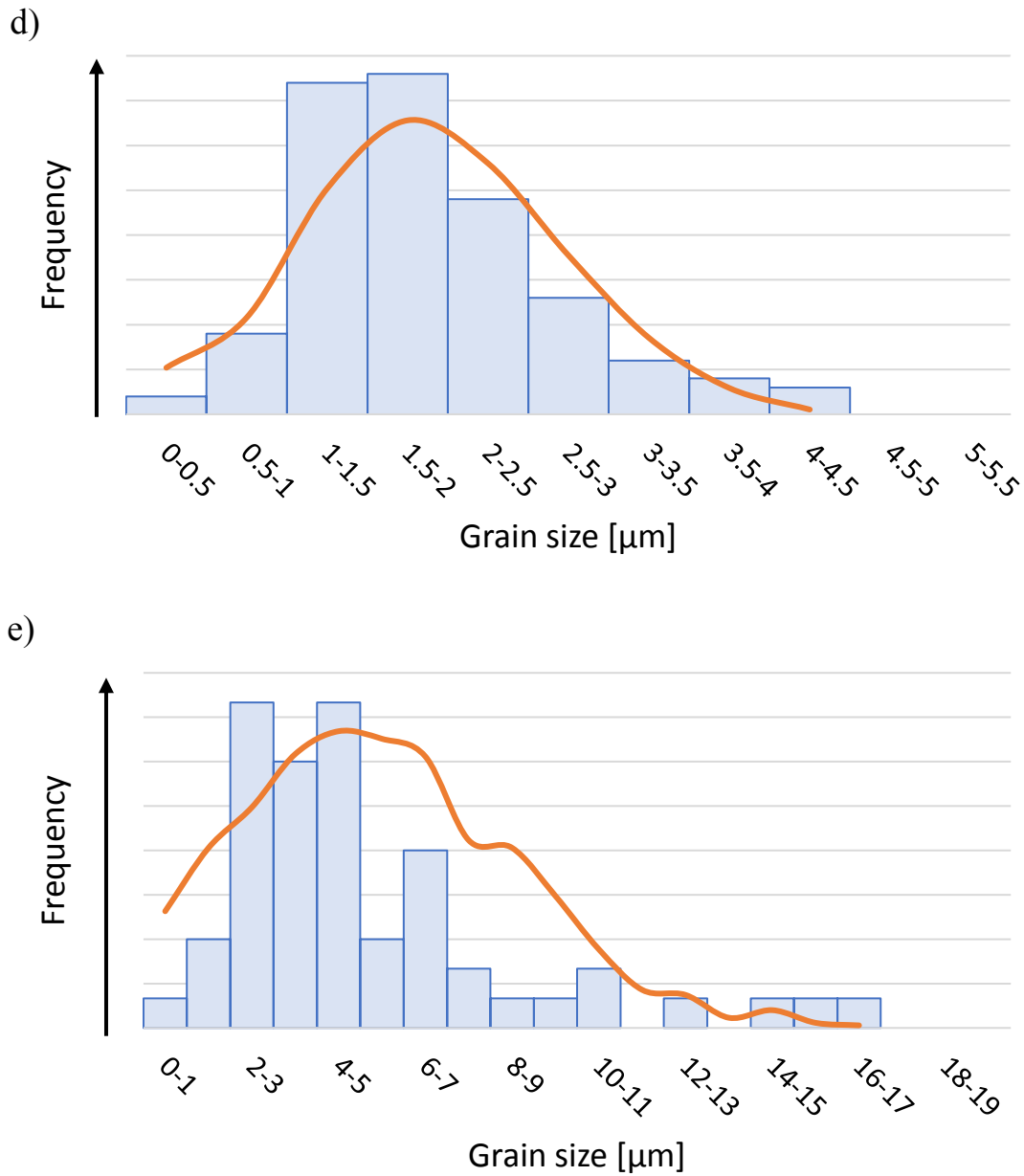


Figure 48: Grain size distribution determined by the lineal intercept procedure according to [45]. a) B1-6Co b) B2-6Co c) B3-6Co d) B4-9.5Co e) B5-9.5Co